Chemical Geology 430 (2016) 45–69

Contents lists available at ScienceDirect

Chemical Geology

journal homepage: www.elsevier.com/locate/chemgeo

The formation conditions of the early Ediacaran cherts, South China

Hanjie Wen [a,*], Haifeng Fan [a,*], Shihong Tian [b], Qilian Wang [c], Ruizhong Hu [a]

[a] State Key Laboratory of Ore Deposit Geochemistry, Institute of Geochemistry, Chinese Academy of Sciences, Guiyang 550002, China
[b] Institute of Mineral Resources, Chinese Academy of Geological Sciences, Beijing 100037, China
[c] State Key Laboratory of Environment Geochemistry, Institute of Geochemistry, Chinese Academy of Sciences, Guiyang 550002, China

ARTICLE INFO

Article history:
Received 17 August 2015
Received in revised form 21 January 2016
Accepted 9 March 2016
Available online 18 March 2016

Keywords:
Silicon isotope
Ge/Si molar ratio
REE
Origin mechanism of chert
Ediacaran seawater conditions

ABSTRACT

During the early Ediacaran, abundant cherts (nodules and bands) were discontinuously hosted by dolostones and mudstones of the Doushantuo Formation (635–551 Ma) in the Yangtze Three Gorges area, South China. The appearance of these cherts correlates with the distribution of acanthomorphic acritarch fossils and is potentially important for the reconstruction of the biogeochemical conditions and oceanic chemistry during the early Ediacaran. However, the formation mechanisms of these cherts are still poorly understood. In this study, silicon isotopes, Ge/Si molar ratios and rare earth element (REE) + Y features are used to constrain the origin mechanism of these cherts, silica geochemical cycling and seawater redox conditions during the Early Ediacaran. Our results suggest that the studied cherts were formed by the replacement of precursor carbonate minerals, which included the dissolution of a siliceous precursor and reprecipitation of microquartz. The positive silicon isotopic composition (typically between 0.4‰ and 1.4‰) and Ge/Si molar ratios ($0.04–0.95 \times 10^{-6}$) indicate a major seawater source of Ge and Si in these cherts with minor detrital and negligible hydrothermal contamination. In the early Ediacaran Ocean, the dissolved silica may be derived from the river input with high $\delta^{30}Si$ values. On the other hand, the output of dissolved silica was controlled by inorganic precipitation, which was subsequently fixed as microquartz in cherts during early diagenesis. During the formation of cherts, the primary REE + Y signals of seawater were preserved with little detrital influence. Meanwhile, the REE + Y patterns, obvious negative Ce anomalies and near modern seawater Y/Ho ratios indicate an oxic marine chemistry during chert formation. This oxic seawater environment may have promoted the observed diversity of Ediacaran biological systems. Finally, temporal variations related to silica sources and silicon isotopic fractionation controls in the cherts and/or ocean were also evaluated.

1. Introduction

Precambrian cherts, which were primarily composed of quartz, have been extensively investigated in order to characterize the environmental conditions of the Early Earth. The origins of these cherts have been established, including recrystallization upon diagenesis of a sedimentary amorphous silica precursor, direct hydrothermal precipitation and silicification of precursor rocks (Knauth, 1994; Maliva et al., 2005; Perry and Lefticariu, 2014 and references therein). The silicification of precursor rocks was particularly dominant in the Precambrian Ocean, in which the dissolved silica concentration was high due to the absence of silica-secreting organisms (Siever, 1992; Maliva et al., 2005).

Widespread cherts (nodules and bands) exist in the Ediacaran Doushantuo Formation (635–551 Ma) from the Yangtze Three Gorges area, South China (McFadden et al., 2009; Xiao et al., 2010; Shen et al., 2011; Liu et al., 2014). These cherts are typically not continuously distributed throughout the Doushantuo Formation; however, they played an important role in controlling the acritarch fossil distribution (McFadden et al., 2008, 2009; Xiao et al., 2010; Liu et al., 2013). Previous studies have reported that abundant acanthomorphic acritarch fossils (e.g., *Tianzhushannia spinosa* assemblage and *Hocosphaeridium scaberfacium*) have been well-preserved in these cherts (Zhang and Knoll, 1998; Zhou and Xiao, 2007; McFadden et al., 2009; Liu et al., 2013, 2014). These fossils are useful tools for the biostratigraphic subdivision and correlation of the Ediacaran system (McFadden et al., 2009; Liu et al., 2013). Moreover, some Ediacaran acanthomorphs may exhibit affinities with early animals. Thus, their distribution can be used to understand the evolution of modern biological systems (Yin et al., 2007). The distribution of these acritarchs in the Doushantuo Formation is commonly associated with the occurrence of cherts (nodules and bands) and phosphates, suggesting a certain degree of preservation bias and/or environmental control (Yin et al., 2007; Zhou and Xiao, 2007; McFadden et al., 2009).

These cherts are of great significance for the interpretation of Early Ediacaran biogeochemical/oceanic conditions (McFadden et al., 2009; Xiao et al., 2010; Fan et al., 2014). However, few studies have focused on their origins and the geochemistry of the early Ediacaran Doushantuo Formation (Xiao et al., 2010; Shen et al., 2011). For instance, carbonate minerals and rim pyrites can be observed in these chert nodules and bands. The sulfur isotopic compositions ($\delta^{34}S_{pyrite}$ = 15.2‰–39.8‰) of

* Corresponding authors.
E-mail addresses: wenhanjie@vip.gyig.ac.cn (H. Wen), fanhaifeng@mail.gyig.ac.cn (H. Fan).

http://dx.doi.org/10.1016/j.chemgeo.2016.03.005
0009-2541/

cherts and the small sulfur isotopic fractionation (<22‰) between coexisting pyrite- and carbonate-associated sulfate (CAS) indicate rapid bacterial sulfate reduction (BSR) during early diagenesis (Xiao et al., 2010). Therefore, Xiao et al. (2010) proposed that the chert nodules were pervasively formed through the replacement of parental carbonate sediments before compaction. In addition, the Ge/Si ratios of these cherts indicated a strong terrestrial influence in the Yangtze basin or a high dissolved organic carbon content in Ediacaran seawater (Shen et al., 2011). Si isotopic data from three Doushantuo Formation cherts was reported by Robert and Chaussidon (2006), however, the main silica source and the silicification mechanism have not been well established.

The Si isotopic compositions, Ge/Si molar ratios and rare earth element constrains of Early Ediacaran Doushantuo Formation cherts (nodules and bands) from five Yangtze Three Gorges area outcrops (sections) were investigated to characterize the Ediacaran chert formation mechanisms, silica geochemical cycling and to reconstruct the Ediacaran seawater redox conditions.

2. Geological setting

The Ediacaran successions on the Yangtze craton were deposited in a southeast-facing passive continental margin. They consist of the Doushantuo and Dengying/Liuchapo Formations, which overlie the glacial diamictites of the Nantuo Formation (Li et al., 1999; Jiang et al., 2007). The age of the Doushantuo Formation has been constrained by the high precision U–Pb zircon dating from volcanic tuff within the base cap carbonate (635 ± 0.6 Ma) and below the Doushantuo/Dengying contact (551.1 ± 0.7 Ma) (Condon et al., 2005).

The Doushantuo Formation ranges from 90 to 200 m thick in the Yangtze Three Gorges area and is generally subdivided into four lithologic members (Zhou and Xiao, 2007; McFadden et al., 2008). Member I is represented by a 5-m-thick cap carbonate (Jiang et al., 2007). Member II is characterized by interbedded black shale and shale dolostone with abundant pea-sized chert nodules that contain microfossils (Zhang and Knoll, 1998; Xiao et al., 2010). Member III contains a 40–60-m-thick layer of medium bedded dolostone with chert bands or lenses. Member IV is an approximately 10-m-thick unit of black organic-rich shale, siliceous shale, and/or mudstone, with mixed large dolomitic concretions (e.g., McFadden et al., 2008; Liu et al., 2013).

This study analyzed five Doushantuo Formation outcrops from the Yangtze Three Gorges area of South China (Fig. 1A). The stratigraphy and lithology of the five outcrops have been described in detail (Fig. 1B, Jiang et al., 2007; Zhou and Xiao, 2007; McFadden et al., 2008; Liu et al., 2013, 2014; Zhu et al., 2013). The Baiguoyuan (BGY, N31°19′31″, E111°03′33″) section is located on the northwestern limb of the Huangling anticline. The Liuhuiwan (LHW, N30°57′11″, E111°16′59″), Niuping (NP, N30°49′53″, E111°09′24″), Jiulongwan (JLW, N30°48′54″, E111°03′20″) and Chenjiayuanzi (CJYZ, N30°49′50″, E111°06′31″) sections are located on the southeastern limb of the Huangling anticline (Fig. 1A). The BGY section was inferred to be a shallow water face and recorded two carbon isotopic negative excursions in the middle of the second sedimentary sequence (BAINCE) and during the third sequence (DOUNCE; Fig. 1B, Zhu et al., 2013; Fan et al., 2014). Only four acritarch fossils (*Cavaspina acuminata*, *Knollisphaeridium maximum*, *Knollisphaeridium triangulum* and *Tanarium conoideum*) have been reported in cherts from Member III of the BGY section (Liu et al., 2013). To date, no acanthomorphic acritarch fossils have been reported in the LHW section. Only one negative carbon isotopic excursion (BAINCE) was observed in the LHW section, which could be equivalent to the first negative carbon isotopic excursion in the BGY section (Fig. 1B, Zhu et al., 2013; Fan et al., 2014). Three remarkable negative carbon isotopic excursions (CANCE, BAINCE, and DOUNCE) were recorded in the JLW and CJYZ sections (Fig. 1B). These negative carbon isotopic excursions can be easily correlated (Jiang et al., 2007; McFadden et al., 2008; Liu et al., 2014). Abundant acanthomorphic acritarch fossils have been preserved in the NP, JLW and CJYZ sections, in which two different biozones can be subdivided into lower assemblages (*T. spinosa*) of Member II cherts and upper assemblages (*H. scaberfacium* and *Hocosphaeridium anozos*) of Member III cherts (McFadden et al., 2009; Liu et al., 2013, 2014).

3. Samples and methods

3.1. Samples

Fresh cherts (nodules and bands) and hosted dolostones were collected from Members II and III of the Doushantuo Formation. The sampling locations are illustrated in Fig. 1B. The diameters of the chert nodules, which are usually hosted by dolostones and mudstones (Member II), range from several millimeters to a few centimeters (Fig. 2A, Xiao et al., 2010). These chert bands exhibit thicknesses of 2–10 cm and are always inter-laminated with dolostones and mudstones (Member III; Fig. 2B, Fan et al., 2014); however, they are not uniformly distributed throughout the Doushantuo Formation (McFadden et al., 2009).

The cherts contain major microquartz minerals and minor residual micritic dolomites (Fig. 2C and Appendix figures). Small amounts of fibrous quartz and megaquartz have been observed in some cherts (Fig. 2D and E). In addition, some cherts contain organic matter, phosphatic grains, authigenic apatite, and disseminated pyrite (a few μm in size) (McFadden et al., 2008; Xiao et al., 2010). These cherts also contain minor Fe-oxide and clay minerals (Fig. 2C and F). Microlaminations in cherts can be traced into the matrix, which indicates that the cherts were not reworked during the post-deposition processes (Xiao et al., 2010). Additional mineralogy details can be found in the Appendix figures.

3.2. Analytical methods

3.2.1. Major and trace elements

Powder samples were mixed with a lithium tetraborate powder in a platinum crucible. The mixture was melted and formed pellets, which underwent high temperature (>1000 °C) glass fusion for 2 h. The major elements were determined using X-ray fluorescence (XRF) at the ALS Chemex (Guangzhou) Co., Ltd. The standard reference materials (SARM-45) were analyzed together with unknown samples, and the obtained precision was better than 5% (Fan et al., 2014).

The trace elements were determined by inductively coupled plasma mass spectrometry (ICP-MS) at the Institute of Geochemistry, Chinese Academy of Sciences (CAS). Powder samples (50 mg) were digested in a PTFE bomb using ultrapure HF and HNO_3 acids under pressure at high temperature (190 °C) for 12 h. After complete digestion and HF-HNO_3 evaporation, the samples were diluted in 3% HNO_3 using a quantitative Rh internal standard solution. The clear solution was analyzed for trace elements and rare earth elements using ICP-MS (Qi et al., 2000). During the analytical processes, the standard reference materials (AGV-2 and AMH-1) were measured together with the samples at REE accuracy of 3% and Ge accuracy of 10%. Our REE and Ge results are consistent with previous data reported by Raczek et al. (2001) and http://georem.mpch-mainz.gwdg.de/sample_query.asp (Appendix tables).

3.2.2. Silicon isotopes

The Si isotope measurement method was described in detail by Ding et al. (1996, 2004, 2011). First, the carbonates and organic carbon must be removed via leaching with HCl and at 500 °C. Subsequently, the residual samples reacted with BrF_5 in a metallic vacuum line to form SiF_4. The SiF_4 gas was then purified using a Cu tube containing Zn particles at 60 °C. The silicon isotopic compositions were analyzed using a MAT-253 gas source isotope ratio mass spectrometer at the Institute of Mineral Resources, CAGS. The silica recovery yielded an average value of 97 ± 4% for all samples. The silicon isotopic compositions are reported as $\delta^{30}Si$ against the NBS-28 reference material. AGV-2 (andesite), as a secondary standard, and our samples were measured together

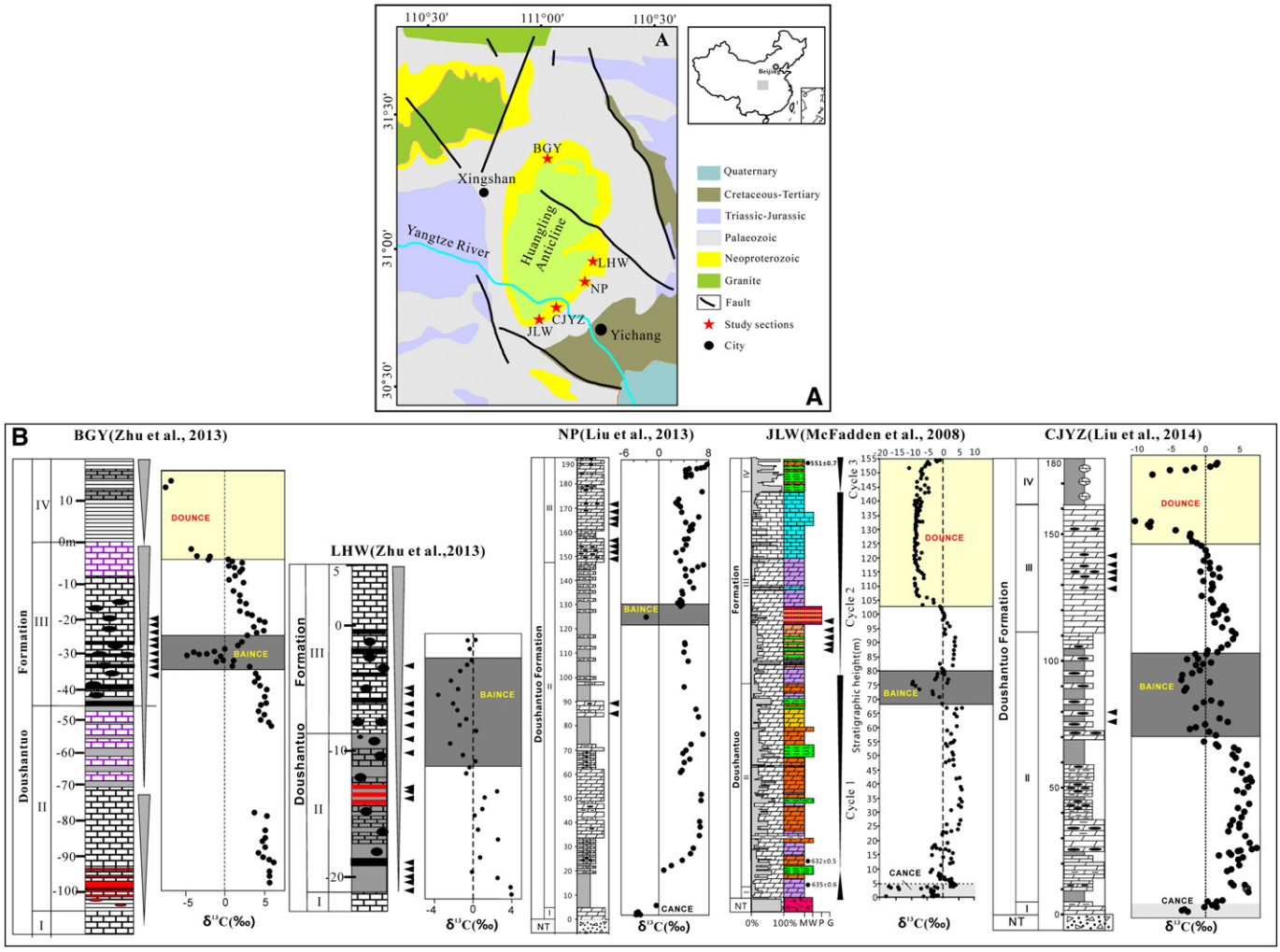

Fig. 1. A. Simplified geological map showing locations of the investigated sections (outcrops) in the Yangtze Three Gorges area, South China. B. The stratigraphic column and carbon isotopic curves of five studied sections, modified from McFadden et al. (2008), Zhu et al. (2013) and Liu et al. (2013, 2014). BGY: Baiguoyuan section, LHW: Liuhuiwan section, NP: Niuping section, JLW: Jiulongwan section, CJYZ: Chenjiayuanzi section. CANCE is a Cap carbonate Negative C isotopic Excursion, which appears in the cap carbonate at the base of the Doushantuo Formation in most sections of the study area (called N1 in Jiang et al., 2007 and EN1 in Zhou and Xiao, 2007 and McFadden et al., 2008). BAINCE is a Baiguoyuan Negative C isotopic Excursion in the middle of the second sequence (Zhu et al., 2013), which corresponds with N2 in Jiang et al. (2007) and EN2 in Zhou and Xiao (2007) and McFadden et al. (2008). DOUNCE is a remarkable Negative C isotopic Excursion that extends from the upper portion of Member III to the basal part of the Dengying Formation (Zhu et al., 2013), which may correspond to the worldwide Ediacaran Shuram–Wonoka anomaly.

with two Chinese national reference materials (GBW04421 and GBW04422). The long-term reproducibility of the two Chinese national reference materials (GBW04421 and GBW04422) was better than ±0.1‰ (2σ) for δ^{30}Si (Li et al., 1995, 2014; Ding et al., 2004, 2011). The δ^{30}Si values of GBW04421 and GBW04422 are 0 ± 0.1‰ and −2.6 ± 0.1‰ in this study, corresponding with data (−0.04 ± 0.1‰ for GBW04421 and −2.58 ± 0.1‰ for GBW04422) published by Ding (2004). The average δ^{30}Si value of AGV-2 is −0.1 ± 0.1‰ (n = 5, 2σ), which is also consistent with previous data (−0.13 ± 0.16‰, Geilert et al., 2014b; −0.14 ± 0.05‰, Zambardi and Poitrasson, 2010).

4. Results

4.1. Major elements

The distribution of major elements is consistent with the mineralogical observations. The SiO_2 contents of all cherts range from 67.3% to 97.7%, with an average of 87.7 ± 8.2% (Appendix Table 1). CaO and MgO are present as minor components, with contents ranging from 0.34% to 10.08% and 0.03% to 5.62%, respectively. Al_2O_3 and Fe_2O_3 also represent minor components, with concentrations ranging from 0.02% to 0.55% and 0.01% to 1.15%, respectively. The P_2O_5 contents in all cherts are relatively low, ranging from 0.01% to 1.60%.

4.2. Rare earth elements

The total rare earth element (TREE) contents in the BGY cherts display a range from 3.4 to 71.7 ppm (Appendix Table 2). The Y/Ho ratios (22–32), with an average of 27 ± 3, are similar to chondritic and super-chondritic values (22–32). REE values were normalized using post-Archean Australian shale (PAAS). All BGY cherts exhibit strong negative Ce anomalies (0.50 to 0.62). The average TREE content in the LHW cherts (11.8 ± 6.2 ppm) is lower than the contents in the BGY cherts. The Y/Ho ratios of the LHW cherts are slightly higher than those of the BGY cherts, with an average of 31 ± 4. Weak negative Ce anomalies (0.65–1.00) are recorded in these LHW samples (Fig. 3). The TREE contents of the NP and JLW cherts are consistent with those of the LHW cherts. The CJYZ cherts contain relatively lower TREE contents (7.01 ± 6.19) compared to other sections. However, these cherts exhibit near seawater Y/Ho ratios of 31–43 for the NP cherts, 33–45 for the JLW cherts, and 30–47 for the CJYZ cherts. Meanwhile, negative Ce anomalies have also been preserved in these cherts (0.60 ± 0.08 for NP, 0.69 ± 0.09 for JLW

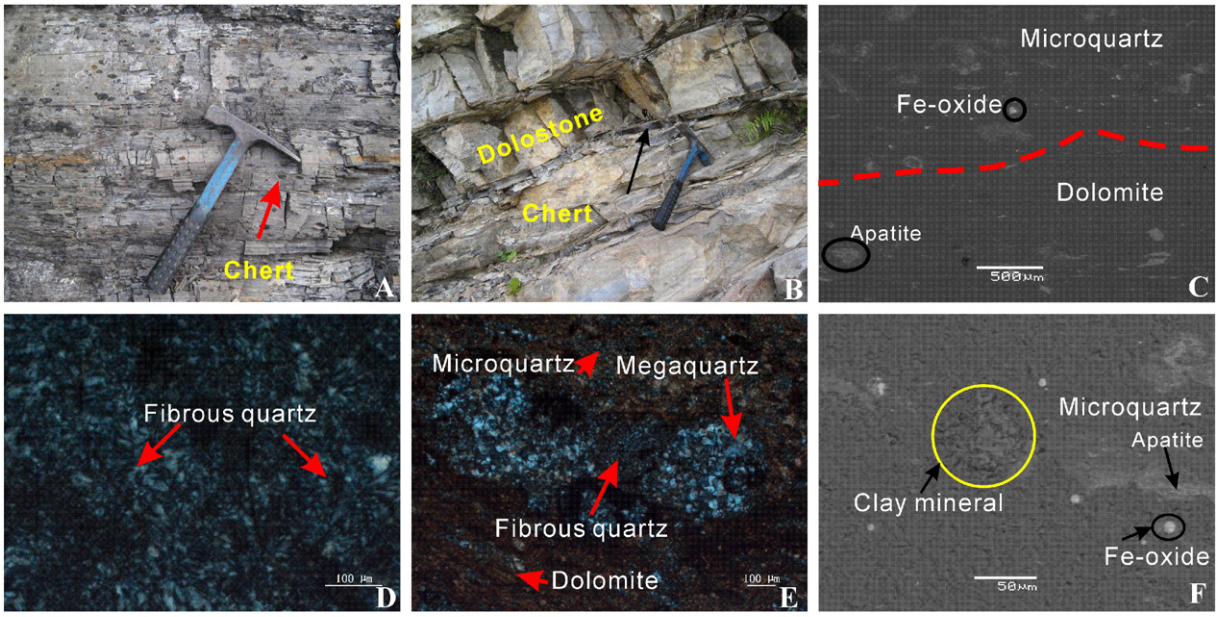

Fig. 2. A. Member II chert nodules from the Jiulongwan section. B. Member III chert bands from the Niuping section. C. Scanning electron microscopy (SEM) micrographs of the major minerals in cherts (LHW-13). D. Optical micrographs of the fibrous quartz in cherts (LHW-25). E. Optical micrographs of micro- and mega-quartz and fibrous quartz in CJYZ cherts (LHW-25). F. Scanning electron microscopy (SEM) micrographs of Fe-oxides and clay minerals in cherts (BGY04). More detailed mineralogy and major element mapping can be found in the Appendix figures.

and 0.66 ± 0.08 for CJYZ). Fig. 3 illustrates the same REE + Y pattern in cherts and some interbedded dolostones from the five studied sections. Samples from the NP, JLW, and CJYZ sections are characterized by a relative depletion of heavy rare earth elements (HREEs) compared to the BGY and LHW cherts.

4.3. Ge/Si molar ratios

The Ge/Si ratios of cherts from the five sections range from 0.04×10^{-6} to 0.95×10^{-6}, with an average of 0.36×10^{-6} (Appendix Table 1). The Ge/Si ratios of the BGY cherts ($0.15–0.62 \times 10^{-6}$) are similar to those of the LHW cherts ($0.09–0.54 \times 10^{-6}$). The most variable Ge/Si ratios are recorded in the JLW ($0.20–0.72 \times 10^{-6}$) and NP cherts ($0.26–0.95 \times 10^{-6}$). These results are mostly lower than the Member II JLW chert results reported by Shen et al. (2011). The narrowest range of Ge/Si molar ratios ($0.04–0.15 \times 10^{-6}$) is recorded in the CJYZ cherts, with an average ratio of $0.10 \pm 0.03 \times 10^{-6}$. The Ge/Si ratios of the majority of the studied cherts are lower than those of the Si-rich (>60% SiO_2) mesobands in the Mesoarchaean Pongola Supergroup ($2.89–7.56 \times 10^{-6}$) (Delvigne et al., 2012), the accepted "average global modern river" value (0.54×10^{-6}, Froelich et al., 1992), and modern seawater (0.72×10^{-6}, Froelich et al., 1985). The broad positive correlations between Ge/Si ratios and Al_2O_3 contents are observed in the five sections (Fig. 4A and B). Note that two distinct trends exist between the Ge/Si ratios and Fe_2O_3 contents, as shown in Fig. 4C and D.

4.4. Silicon isotopes

Thirty cherts from three sections (BGY, LHW and NP) were analyzed for silicon isotopes. Their $\delta^{30}Si$ values range from −0.5‰ to 1.4‰ (Appendix Table 1). The BGY cherts exhibit two groups of bimodal silicon isotopic compositions: a lower group from −0.5‰ to −0.3‰ and a higher group from 0.8‰ to 1.1‰. The $\delta^{30}Si$ values of the LHW chert vary from 0.4‰ to 1.4‰, and mainly fall between 0.9‰ and 1.4‰, with an average of 1.0 ± 0.3‰ (1 SD). Excluding two samples (NP-1 and NP-2), the $\delta^{30}Si$ values of the NP chert fall within the narrow range of 0.7‰ to 1.0‰, with an average of 0.8 ± 0.2‰ (1 SD). Most $\delta^{30}Si$ values are positive and generally higher than the average continental crust value (−0.25 ± 0.16‰, Ding et al., 1996; Savage et al., 2013) and the Mesoarchaean Pongola Supergroup Si-rich (>60% SiO_2) mesobands values (−2.27 to −0.53‰, Delvigne et al., 2012). Our $\delta^{30}Si$ values encompass a narrower range than those of cherts from the old Akademikerbreen Group (750–800 Ma), Spitsbergen (−1.38 ± 0.09‰ to +1.26 ± 0.03‰) reported by Chakrabarti et al. (2012) and the Doushantuo Formation cherts (−1.27 ± 0.89‰ to +2.89 ± 0.39‰) reported by Robert and Chaussidon (2006).

5. Discussion

5.1. The diagenetic chert model

Modern cherts are commonly formed via the transformation of amorphous opal-A to opal-CT to microquartz by dissolution–reprecipitation reactions, although opal-A can be converted to microquartz without the opal-CT intermediate phase when the silica concentration remains below the opal-CT solubility (Knauth, 1994; DeMaster, 2014; Perry and Lefticariu, 2014). Residual opal-A and opal-CT in modern cherts may imply incomplete transformation. However, Precambrian primary cherts were formed via inorganic pathways due to the absence of silicifying organisms, including several dissolution–reprecipitation steps from an amorphous silica precursor during diagenesis (Siever, 1992; Marin-Carbonne et al., 2012, 2014; Perry and Lefticariu, 2014; Stefurak et al., 2015). Most reports have also proposed that Neo- and Mesoproterozoic cherts were primarily formed via the diagenetic replacement of carbonates in nodules and/or discontinuous bands, while Archean and Paleoproterozoic cherts can be formed by the direct precipitation of quartz or siliceous gels from silica saturated seawater due to the absence of silicifying organisms (Siever, 1992; Knauth, 1994; Maliva et al., 2005; Perry and Lefticariu, 2014 and references therein).

Our cherts typically occurred as discrete nodules and bands within dolostone formations. The preservation of inclusions and carbonate precursor ghosts suggests that silica selectively replaced carbonate skeletons. The detailed petrographic features indicate that carbonate was preferentially replaced compared to apatite. The disseminated pyrite is randomly distributed and considered to be early diagenetic in origin (Xiao et al., 2010). These characteristics are similar to those of the Phanerozoic carbonate-replacement cherts and Precambrian peritidal cherts (Maliva et al., 2005). The observation of fibrous quartz and megaquartz

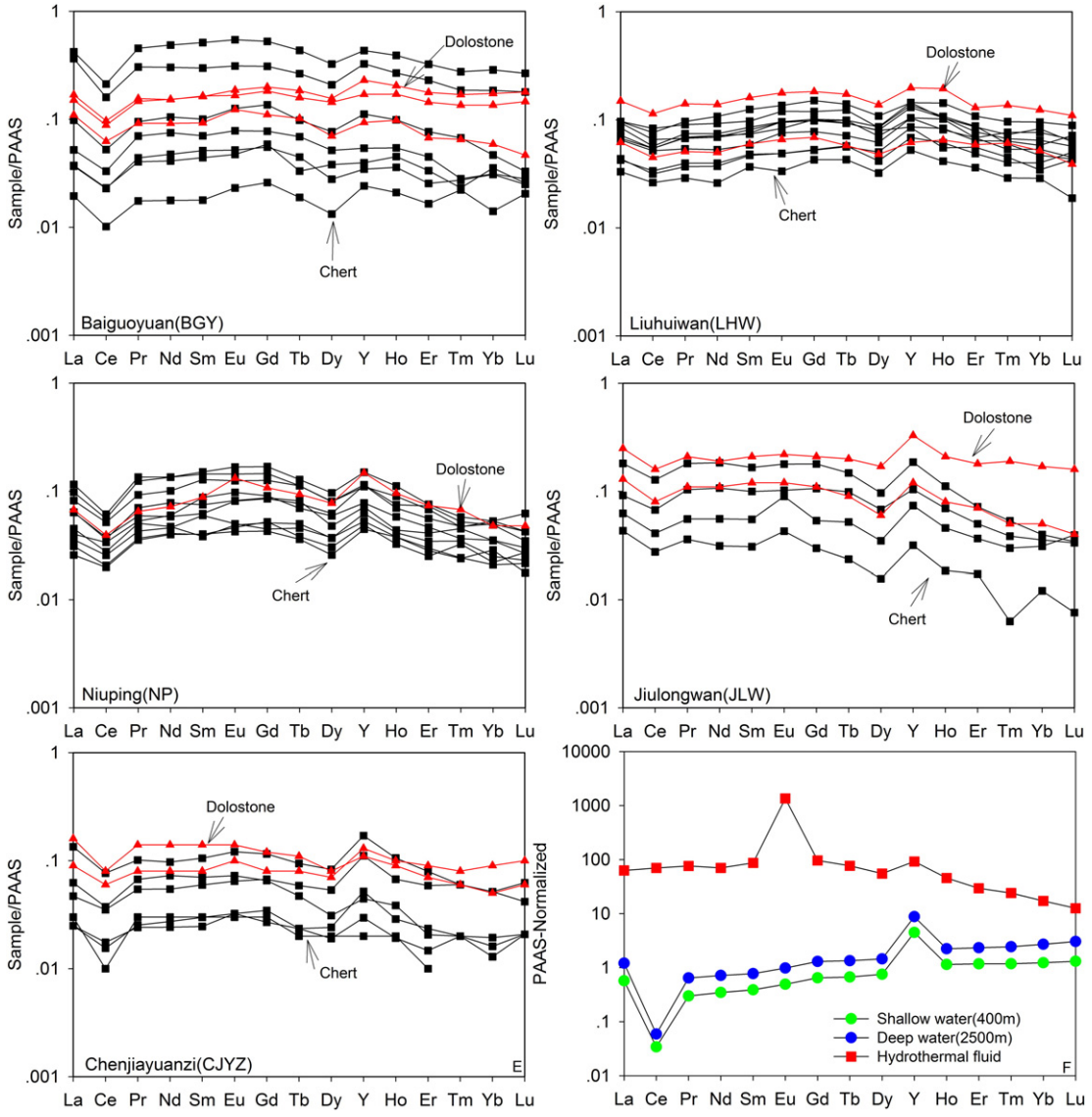

Fig. 3. PAAS-normalized REE + Y patterns of cherts and inter-laminated dolostones from the five investigated sections (A, B, C, D and E), which exhibits negative Ce anomalies and HREE-depletion compared to LREEs and MREEs. The undistinguished REE + Y patterns in cherts and interbedded dolostones indicate that the REE pattern was not significantly altered during silicification. The REE + Y patterns of hydrothermal fluids and modern seawater are also plotted in F, in which the data is cited from Bau and Dulski (1999) and Alibo and Nozaki (1999).

indicates the transformation of amorphous siliceous gel to fibrous and/or microquartz, which may occur during the dissolution of microquartz and reprecipitation of megaquartz in early diagenesis (Fig. 2D and E). The microlaminations in the matrix and wrapped around the chert nodule suggest that carbonate was silicified before compaction (Xiao et al., 2010), which can be confirmed by scanning electron microscopy (SEM) mapping (Appendix figures). Based on our observations, these cherts could have been formed by the replacement of carbonate during very early diagenesis and before compaction, where slightly acidic pH conditions could play an important role in dissolving carbonate and aggregating of silica via polymerization (Stefurak et al., 2015 and references therein). Subsequently, amorphous siliceous gel precipitated from seawater or pore water would be converted into fibrous quartz and/or micro- and megaquartz via dissolution–reprecipitation processes.

5.2. REE geochemistry

5.2.1. Detrital and diagenetic effects

Detrital materials potentially affected the REE + Y patterns of carbonates and cherts due to the high TREE contents in silicate minerals. The Al, Sc, and Zr contents and the relationship between these elements and TREE are commonly applied to monitor continental silicate detritus contamination (Nothdurft et al., 2004; Ling et al., 2013). The positive correlation between the TREE and Al_2O_3 contents of the NP cherts suggests that the higher TREE and Al_2O_3 contents can be explained by a mixing of seawater and continental materials (Fig. 5A). Two BGY cherts with the highest TREE value (51.6 and 71.7 ppm) and chondritic Y/Ho ratios (28 and 31) display evidence of significant detritus contamination. The differing trends between the TREE and Al_2O_3 contents in the NP and BGY cherts may suggest other influences, such as different clay mineral and diagenetic phosphate REE contents. The absence of positive correlations between the TREE and Al_2O_3 contents, in addition to the lower TREE and Al_2O_3 contents in the LHW, JLW and CJYZ cherts, indicates a negligible detrital input. This geochemical evidence is consistent with mineralogical observations, in which more clay minerals are present in cherts with high Al_2O_3 contents (Fig. 2 and Appendix figures). On basis of previous studies (Nothdurft et al., 2004; Ling et al., 2013) and our results, a criteria (Al_2O_3 > 0.3%, Sc > 2.0 ppm, TREE > 20 ppm) is applied to define the significant detrital contamination. Therefore, these samples exhibiting significant detrital contamination were excluded from the following discussion.

Shields and Stille (2001) proposed that diagenesis could cause REE patterns to become progressively Ce-enriched, Eu-depleted and Dy_N/

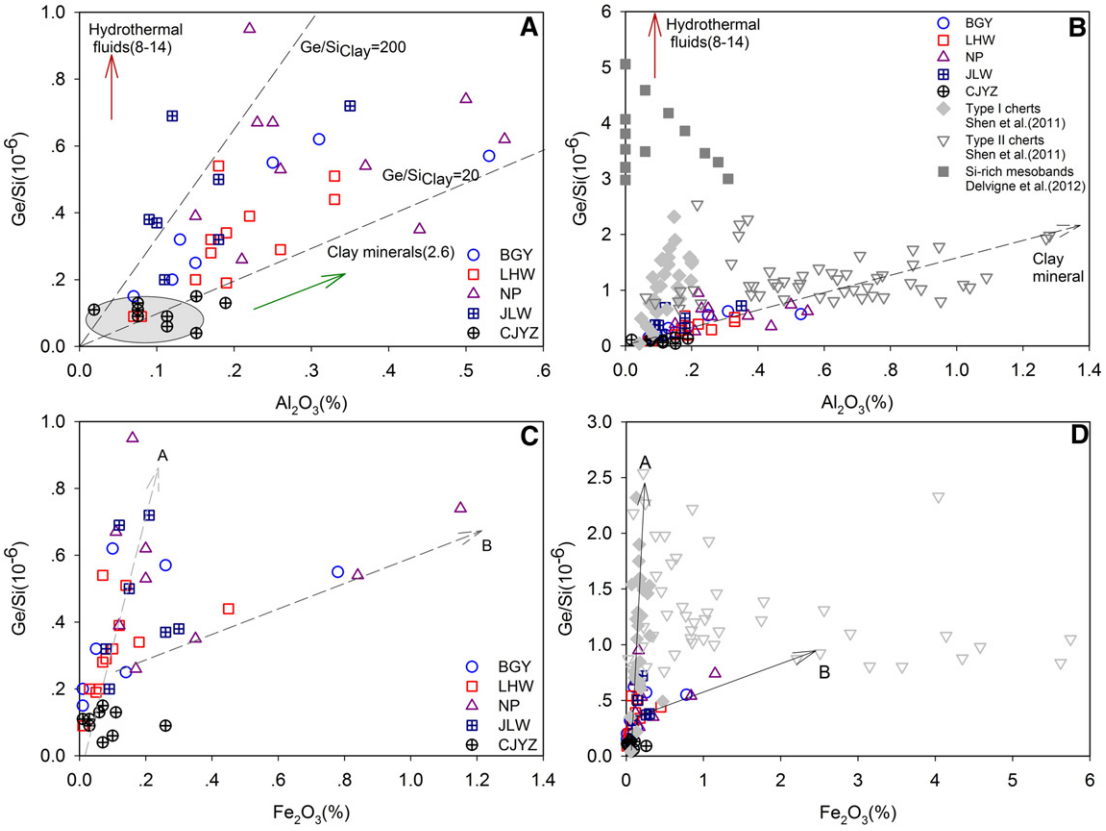

Fig. 4. Plots of Ge/Si ratios versus Al_2O_3 and Fe_2O_3 contents from the studied cherts, and compared with the published JLW chert nodule (Shen et al., 2011) and Si-rich mesoband data (Delvigne et al., 2012). A and B indicate a normal mixing model between pure cherts and clay minerals for the studied cherts, while samples from Shen et al. (2011) are mainly Type-II cherts with abundant disseminated pyrite. However, Type-I cherts with less disseminated pyrite and Si-rich mesobands may reflect the special mixing of Fe-oxides and hydrothermal fluids with extremely high Ge/Si ratios. C and D suggest an important adsorption of Ge by Fe oxides and/or co-precipitation with Fe hydroxides. Trend B in (D) may imply a rapid Fe-oxide increase due to the oxidation of Fe (II) via anoxic deep-water upwelling into oxic shallow water. The broad negative correlation in Si-rich mesobands may reflect the co-precipitation of dissolved Si with Fe-hydroxides.

Sm_N depleted, although REEs in carbonates and cherts are not easily altered after deposition (Webb et al., 2009). However, a negative correlation between Ce/Ce* and Dy_N/Sm_N ratios has not been observed in cherts and dolostones (Fig. 5B), indicating that the REE + Y patterns and Ce anomalies of the studied cherts and dolostones have not shifted during the diagenetic processes.

5.2.2. REE patterns of cherts

The REE + Y patterns of the studied cherts are similar to those of the dolostones reported by Ling et al. (2013), who extracted the REEs associated with carbonate minerals in dolostones using 1 M acetic acid. The apparent negative Ce anomalies of the cherts in this study are similar to those of "typical seawater" (Fig. 3), which suggests that the cherts preserved the oxic, seawater-like REE + Y patterns. A recent study has also suggested an oxic condition for these cherts on the basis of near zero Fe isotopic composition (Fan et al., 2014). The cherts analyzed in this study and the carbonates studied by Ling et al. (2013) exhibit HREE depletion compared to modern oxic seawater, which can be attributed to the decreasing carbonate–seawater partition coefficients of REEs with increasing atomic number (Zhong and Mucci, 1995; Ling et al., 2013). However, one additional explanation suggested that ocean redox conditions play an important role in controlling HREE contents in seawater. The strong adsorption of REEs by Fe–Mn oxyhydroxides results in lower light rare earth element (LREE) contents, high HREE contents and strong negative Ce anomalies in oxic modern seawater (Sholkovitz et al., 1994; Bau et al., 1996). In modern dysoxic and anoxic water columns, the dissolution of Fe- and Mn-oxyhydroxides can increase LREE and middle rare earth element (MREE) contents by as much as ten times (German et al., 1991; Sholkovitz et al., 1992). A redox-stratified oceanic model during the formation of the Doushantuo Formation was proposed by Li et al. (2010). In this model, oxic shallow water coexisted with ferruginous deep water, while euxinic conditions often prevailed at the shelf. Under these conditions, redox processes would increase the LREE and MREE concentrations relative to the HREE concentrations in anoxic deep water. This may explain the HREE-depleted patterns, particularly those in the NP, JLW, and CJYZ cherts. Meanwhile, the strong REE adsorptions exhibited by the Fe–Mn oxyhydroxides in oxic shallow water columns resulted in strong negative Ce anomalies in the BGY cherts. However, the apparent negative Ce anomalies that imply oxic conditions are inconsistent with the anoxic conditions indicated by the HREE-depletion in the NP, JLW, and CJYZ cherts. Following the primary REE + Y patterns (HREE-depletion) of carbonates (e.g., Ling et al., 2013) and phosphorites (e.g., Emsbo et al., 2015), the Ediacaran shallow seawater may be characterized by weak negative Ce anomalies and an HREE-deplete pattern, compared to the modern seawater, which may be attributed to the mixing of the upwelling ferrugenious deep water with higher LREE and lower HREE concentrations than shallow water.

Unlike Ce and LREEs, Y is removed from seawater by particle surface reactions at rates that can be two times slower than Ho removal. This could induce higher Y/Ho ratios (44–83) in oxic shallow marine environments relative to typical shale compositions (~30, Bau et al., 1997; Nozaki et al., 1997). However, the Y/Ho ratios in modern suboxic and anoxic waters decreased from 83 to <30 because of an increase in Ho as Fe–Mn oxyhydroxides dissolved (Bau et al., 1997). Continental detrital contamination can also lower the Y/Ho ratios of chemically precipitated sediments because detritus commonly displays uniform and low Y/Ho ratios (26–27) (Nozaki et al., 1997), which has been discussed in Section 5.2.1. Therefore, the high Y/Ho ratios (≥40) in the studied cherts

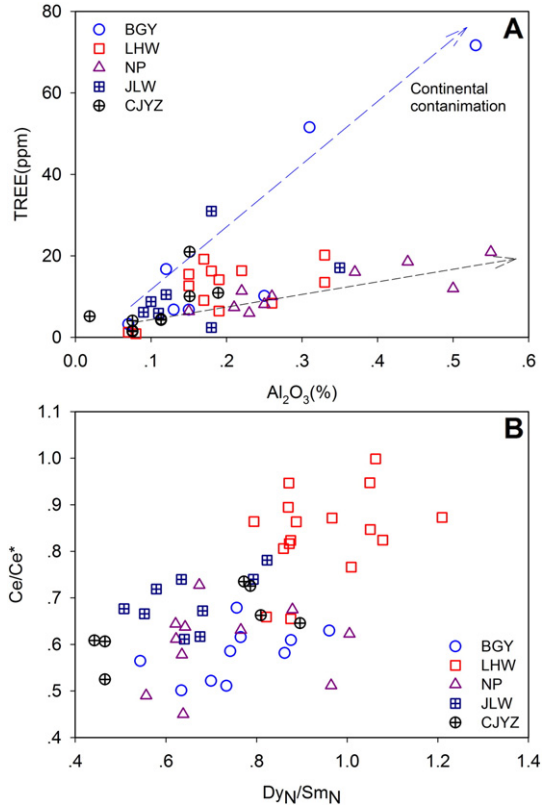

Fig. 5. A. The relationship between total rare earth elements (TREE) and Al_2O_3 contents suggests that significant continental contamination occurred for two BGY cherts (BGY-4 and 5) and a few LHW and NP cherts. B. The absence of a negative Ce/Ce* correlation with Dy_N/Sm_N implies that the REE + Y patterns and Ce/Ce* were not significantly altered during the diagenetic processes.

may reflect the strong scavenging of Ho by Fe–Mn oxyhydroxides in an oxic seawater above the Fe–redox interface. The relatively low Y/Ho ratios (30 to 40) in those cherts without the significant detrital contamination, may suggest the significant mixing by the upwelling ferrugenious deep water with low Y/Ho ratios.

Thus, the main REE source in our cherts is derived from Ediacaran seawater, with different magnitudes of terrigenous contamination. The cherts preserved the primary REE + Y patterns of Ediacaran seawater, and the obvious negative Ce anomalies and super-chondritic Y/Ho ratios (up to 47) of our cherts suggest an oxic seawater condition during chert deposition.

5.3. Using Ge/Si molar ratios to trace Ge and Si sources

The distinct geochemical characteristics of Si and Ge resulted in vastly different Ge/Si ratios in modern river and hydrothermal fluids (e.g., $(Ge/Si)_{river} = 0.54 \times 10^{-6}$ and $(Ge/Si)_{hydrothermal} = 11 \pm 3 \times 10^{-6}$) (Froelich et al., 1992; Mortlock et al., 1993). Therefore, the Ge/Si ratios preserved in marine cherts can be applied to determine Ge and Si behaviors and sources in ocean environments.

5.3.1. Diagenetic effects

Most authors have suggested that the redistribution of Ge in pore waters and sediments was dominantly controlled by the dissolution of diatoms and opal-A, along with the removal of near-surface reducing sediments during early diagenesis (King et al., 2000; Hammond et al., 2000, McManus et al., 2003). They also proposed that near-surface reducing sediments with high Fe^{2+} pore water contents can sequester 55% of the Ge released by opal dissolution. However, anoxic sediments with little pore water Fe^{2+} cannot fractionate Ge/Si ratios from the pore water ratios (Hammond et al., 2000, McManus et al., 2003). We assume that the amorphous siliceous gel may preserve a constant Ge/Si ratio during initial precipitation processes. The dissolution of amorphous siliceous gel during early diagenesis can release much more Ge than Si into pore water, which may result in the lower Ge/Si ratios in the residual solid siliceous gel phase (Hammond et al., 2000, McManus et al., 2003). Subsequently, the Ge released from the dissolution of amorphous siliceous gel can be sequestered during quartz crystallization invoking an important Ge discrimination against Si (Evans and Derry, 2002), which may produce much lower Ge/Si ratios in those recrystallized quartz without the adsorption of Fe-oxide and clay minerals. The repeated dissolution and reprecipitation may explain the lowest Ge/Si ratios, which were observed in the CJYZ cherts with low Fe_2O_3 and Al_2O_3 contents, and the highest ratios, which were displayed by cherts with high Fe_2O_3 and Al_2O_3 contents.

5.3.2. The mixing of Ge-rich clay minerals

The effective Ge discrimination by inorganic opal precipitation would result in near zero Ge/Si ratios in the pure cherts (Evans and Derry, 2002). Conversely, clay minerals often display higher Ge/Si ratios, which are typically $>2 \times 10^{-6}$ (Mayer et al., 2004). The highest Ge/Si ratios (up to 14×10^{-6}) are preserved in mid-ocean ridge hydrothermal fluids (Froelich et al., 1992). In a previous study, the elevated Ge/Si ratios in the JLW cherts were explained by Al-rich component mixing, rather than hydrothermal fluids (Shen et al., 2011). The broad positive correlations between the Ge/Si ratios and Al_2O_3 contents have also been observed in the BGY, LHW and NP sections (Fig. 4A and B), which can be explained by the binary mixing between pure chert end-members with near zero Ge/Si ratios and Al-rich end-members with higher Ge/Si ratios. The first end-member (pure chert) is represented by the CJYZ cherts, which exhibit the lowest Ge/Si ratio (0.10×10^{-6}) and Al contents (0.06%). The second end-member (Al-rich) is represented by the cherts that contain clay minerals (BGY04 and NP10; Fig. 2 and Appendix figures). The different slopes in Fig. 4A reflect Ge/Si ratio variations in clay minerals, where anomalously high Ge/Si values of clay minerals may be due to the formation of secondary clay mineral in pore water with an extremely high Ge/Si ratio (Shen et al., 2011).

5.3.3. The adsorption of Ge-rich Fe-minerals

Experimental studies have suggested that Ge adsorption on Fe-oxides and co-precipitation with Fe (III) hydroxides can also effectively fractionate Ge by a factor of 7 relative to Si in natural sedimentary systems with pH >4 (Pokrovsky et al., 2006). A clear positive correlation exists between the Ge/Si ratios with Fe_2O_3 contents of the studied cherts and the type I cherts in Shen et al. (2011) (Fig. 4C, D), suggesting Ge fractionation relative to Si via the adsorption of Ge on Fe oxides and co-precipitation with Fe (III) hydroxides. The same positive correlations were observed in the pristine BIF of the ca. 2.5 Ga Dales Gorge Member, Hamersley Group, Western Australia (Hamade et al., 2003), the BIF from the ca. 3.7–3.8 Ga Isua Greenstone belt, West Greenland (Frei and Polat, 2007) and the Fe-rich (>60% Fe_2O_3) mesobands in the ca. 2.9-Ga Mesoarchaean Pongola Supergroup, South Africa (Delvigne et al., 2012). However, the Ge/Si ratios and Fe_2O_3 contents of the cherts in this study are much lower than those of the Archean Si-rich mesobands (Fig. 4B).

Two significantly different trends can be observed between the Ge/Si ratios and Fe_2O_3 contents in Fig. 4C and D. Trend A reflects a Fe-bearing clay mineral mixing, given the low total Fe content. There are three possible interpretations of trend B: 1) Ge adsorption and co-precipitation onto Fe-oxides in an oxic marine condition; 2) elevated Fe input due to the upwelling of ferruginous deep water (Fan et al., 2014); or 3) variable fractionation factors between Fe-minerals (Fe-oxyhydroixide/pyrite) and water during Ge adsorption and co-precipitation, which have not been experimentally proven. Although the third hypothesis cannot be excluded based on our data, the first and second hypotheses can easily explain trend B in Fig. 4D. Fe is mainly present as Fe-oxides and negligible pyrite in our cherts (Fig. 2 and Appendix figures). Therefore, the coupled increase of (Trend B) Fe_2O_3 and Ge/Si ratios likely occurred in an oxic

shallow water environment (Fig. 4C). However, the decoupled Fe_2O_3 and Ge/Si ratio variations (Fig. 4D) may result from the oxidation of a massive Fe^{2+} upwelling from ferruginous deep water (Fan et al., 2014).

Therefore, the lowest Ge/Si ratios in the CJYZ cherts resulted from diagenesis. However, the highest values may have been controlled by clay mixing and adsorption onto Fe-bearing minerals. In addition, the highest Ge/Si ratios are significantly lower than those of the hydrothermal end-member, indicating that the Ge and Si sources in the studied cherts were mainly derived from seawater.

5.4. Silicon isotopic composition

5.4.1. The main silica source

The relationships between $\delta^{30}Si$ and the Al_2O_3, TiO_2 and K_2O contents were applied to identify the main silica source and the origin mechanism of ancient cherts (van den Boorn et al., 2007, 2010; Marin-Carbonne et al., 2012; Ramseyer et al., 2013). Three possible quartz components or Si-bearing precursors can be easily identified in Fig. 6. One silica end-member represents hydrothermal fluids with low Al_2O_3, TiO_2 and K_2O contents, a high Ge/Si ratio and a negative $\delta^{30}Si$ value. Many Archean cherts of hydrothermal origin fall in this region (van den Boorn et al., 2007, 2010; Marin-Carbonne et al., 2012). Another end-member represents continental detritus and/or volcanic precursors with high Al_2O_3, TiO_2 and K_2O contents, a moderate Ge/Si ratio and a near zero $\delta^{30}Si$ value. The last end-member is diagenetic quartz that is derived from seawater with low Al_2O_3, TiO_2 and K_2O contents, a low Ge/Si ratio and a typically positive $\delta^{30}Si$ value.

Two BGY cherts display $\delta^{30}Si$ values similar to those of the Archean chemical cherts precipitated from hydrothermal fluids (Fig. 6A). However, these two cherts exhibit significantly lower Ge/Si ratios than hydrothermal fluids, apparent negative Ce anomalies, higher Al_2O_3, Fe_2O_3 and TREE contents, and chondritic Y/Ho ratios. These observations suggest that the low $\delta^{30}Si$ values may be affected by detrital clay minerals and that the hydrothermal contribution is negligible for these two cherts. This deduction can be explained by previous experiments, in which secondary and authigenic clay minerals often exhibit negative $\delta^{30}Si$ values ($\Delta^{30}Si_{(clay-aqueous)} = -0.2$ to $-2.2‰$, Ziegler et al., 2005; Opfergelt et al., 2010, 2012; Pogge von Strandmann et al., 2012).

The other cherts mainly possess low Al_2O_3 contents, low Ge/Si ratios and positive $\delta^{30}Si$ values (0.4‰ to 1.4‰) (Fig. 6). These values are consistent with ca. 540 Ma organism-rich laminated cherts from the South Oman Salt Basin ($Ge/Si < 0.25 \times 10^{-6}$, $\delta^{30}Si = 0.83 \pm 0.28‰$, Ramseyer et al., 2013) and 1.88-Ga Gunflint cherts ($Al_2O_3 < 300$ ppm, $\delta^{30}Si = +2 \pm 1‰$, Marin-Carbonne et al., 2012). Conversely, they are remarkably different from the Si-rich (>60% SiO_2) mesobands in the ca. 2.9 Ga Mesoarchaean Pongola Supergroup, South Africa ($Ge/Si = 2.89$ to 7.56×10^{-6}, $\delta^{30}Si = -2.27$ to $-0.53‰$, Delvigne et al., 2012). The wide range $\delta^{30}Si$ value may be controlled by silica precipitation and the adsorption onto the Fe-oxyhydroxide from a silica-rich seawater strongly influenced by continent-derived freshwaters (Delvigne et al., 2012). The NP cherts display higher Al_2O_3 and Ge/Si ratios and lower $\delta^{30}Si$ values than the LHW cherts (Fig. 6B), which may reflect the binary mixing of: 1) minor continental detritus with higher Al_2O_3 and Ge/Si ratios and near zero $\delta^{30}Si$ values; and 2) major seawater deposition with lower Al_2O_3 and Ge/Si ratios and positive $\delta^{30}Si$ values. These observations suggest that the main silica source is seawater deposition with minor continental detrital/volcanoclastic deposition and hydrothermal contamination, which also reinforces the diagenetic carbonate replacement.

5.4.2. Silicon isotopic fractionation during chert formation

For the studied cherts, the diagenetic origin is described as carbonate replacement during very early diagenesis and before compaction. Two processes associated with the variable $\delta^{30}Si$ values in our cherts are discussed in detail: 1) the precipitation of amorphous siliceous gel from seawater; and 2) the dissolution of amorphous siliceous gel and recrystallization of micro- and megaquartz during diagenesis.

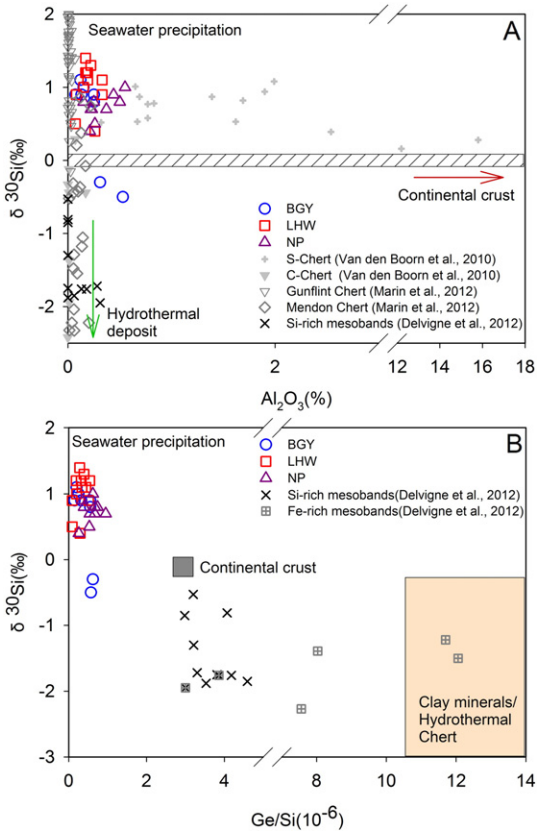

Fig. 6. A. Correlation between $\delta^{30}Si$ values and Al_2O_3 contents in cherts, in which three different silica end-members can be recognized as (1) a seawater deposit with a low Al_2O_3 content and positive $\delta^{30}Si$ values, (2) continental/volcanic materials with a high Al_2O_3 content and near zero $\delta^{30}Si$ values, and (3) a hydrothermal deposit with a low Al_2O_3 content and negative $\delta^{30}Si$ values. S-Chert: silicified precursor chert; C-Chert: chemical chert precipitated from hydrothermal fluids mixing with seawater (van den Boorn et al., 2007). B. Cross-plot of $\delta^{30}Si$ values versus Ge/Si ratios, where three possible silica end-members can be identified as seawater, continental/volcanic materials and clay mineral/hydrothermal fluids. This figure indicates that the silica source in most studied cherts can be derived from seawater, rather than volcanic materials and clay mineral/hydrothermal fluids. The continental crust silica source is cited from Wheat and McManus (2008) and Savage et al. (2013). The hydrothermal and clay silica sources are cited from Mortlock et al. (1993), Shen et al. (2011), Opfergelt et al. (2010) and van den Boorn et al. (2010).

The silicon isotopic fractionation during the inorganic precipitation of dissolved silica is partially dependent on the precipitation rate, composition, and temperature of the ambient solution (Abraham et al., 2011; Oelze et al., 2014, 2015; Geilert et al., 2014a, 2015; Roerdink et al., 2015). The rapid precipitation of dissolved silica as amorphous siliceous gel often produces large silicon isotopic fractionations of $\Delta^{30}Si_{(solid-aqueous)} = -2.0‰$ to $-1.0‰$, resulting in precipitated siliceous solids with low $\delta^{30}Si$ values (Li et al., 1995; Basile-Doelsch et al., 2005; Geilert et al., 2014a). The adsorption of Fe-oxide can also produce a similar fractionation of $-1.2‰$ to $-1.5‰$ (Delstanche et al., 2009). Recent experiments have suggested that large kinetic fractionations occurred during early Al-hydroxide adsorption and co-precipitation, with $\Delta^{30}Si_{(solid-aqueous)} = -1.8$ to $-5.0‰$, which increased with the initial silica concentration during the first 20 days of the adsorption experiment. As the runtime increased, $\Delta^{30}Si_{(solid-aqueous)}$ approached 0‰ (Oelze et al., 2014, 2015).

In contrast, the silicon isotopic fractionations during the dissolution of biogenic and abiogenic silica have not been well established (Demarest et al., 2009; Wetzel et al., 2014; Geilert et al., 2014a). A constant fractionation of $\Delta^{30}Si_{(solid-aqueous)} = +0.55‰$ associated with the dissolution of diatom opal was reported by Demarest et al. (2009), who also proposed that the magnitude is independent of the source material compositions and temperature at which the dissolution occurred. However, a larger $\Delta^{30}Si_{(solid-aqueous)} = -1.1‰$ fractionation at 10–30 °C was

observed during the dissolution of abiogenic amorphous silica (Geilert et al., 2014a). Natural studies indicated that early diagenetic microquartz typically exhibit higher $\delta^{30}Si$ values than late-stage microquartz (Stefurak et al., 2015). However, no isotopic fractionation exists when the precursor is completely dissolved. The wide range of microquartz $\delta^{30}Si$ values may be attributed to a Rayleigh fractionation during reprecipitation processes in a closed system (Marin-Carbonne et al., 2012, 2014).

The Fe/Si and Al/Si ratios of the cherts in this study are much lower than those of Archean cherts. Thus, the siliceous precursors in our cherts may have been formed by the primary inorganic chemical deposition of dissolved silica from seawater rather than by the adsorption of Al- and Fe-oxyhydroxide particles. No concentric growth zones were observed in chert nodules. Consequently, Xiao et al. (2010) suggested that silica precipitation rapidly occurs in the Ediacaran Ocean, which may result in lower $\delta^{30}Si$ values in the siliceous precursor compared to seawater based on the above mentioned fractionation ($\Delta^{30}Si_{(solid\text{-}aqueous)} = -2.0‰$ 2.0‰ to −1.0‰). The $\delta_{30}Si$ values in this study fall within the range of $\delta^{30}Si$ values (−1.27‰ to 2.89‰) measured by Robert and Chaussidon (2006) using SIMS. Our $\delta^{30}Si$ range in whole rocks and the extremely variable $\delta^{30}Si$ range in microquartz from Robert and Chaussidon (2006) may reflect diagenetic alteration during multiple dissolution and recrystallization stages.

5.5. Silica cycling and marine redox conditions during the early Ediacaran

The silica cycling and marine redox conditions in the Ediacaran Ocean are summarized in Fig. 7. Based on our data, the main silica source of the Ediacaran Ocean was determined to be a river flux with minor detrital and hydrothermal fluxes. The strong continental weathering after Nantuo (Marinoan) glaciation may produce high $\delta^{30}Si$ values in river dissolved silica. In this context, the removal of dissolved silica in seawater is controlled by inorganic chemical deposition, in which an approximately −1.5‰ silica isotope fractionation is based on the estimated 20–30 °C seawater temperature (Meng et al., 2011; Geilert et al., 2014a). During diagenesis, the siliceous precursor was completely dissolved, producing no net silicon isotopic fractionation and high silica contents in pore water. When the quartz silica concentration becomes saturated in pore water, the reprecipitation of quartz and replacement of carbonate occur under slightly acidic pH conditions (Stefurak et al., 2015 and references therein). If the siliceous precursor was completely transformed into microquartz and/or fibrous quartz, the primary silicon isotope of the siliceous precursor would be preserved in the entire rock sample in a closed system. However, the micrometer-scale heterogeneous silicon isotopic composition can be observed in microquartz (Robert and Chaussidon, 2006).

A significant continental detritus contribution is preserved in the BGY cherts, corresponding to oxic shallow water conditions associated with the negative Ce anomalies (0.50–0.68), near chondritic Y/Ho ratio (22–32), the paleo-geographic reconstruction and Fe isotopic records (Zhu et al., 2013; Fan et al., 2014). The BGY cherts in Member III of the Doushantuo Formation contain rare acritarch fossils, such as *C. acuminata*, *K. maximum*, *K. triangulum*, and *T. conoideum* (Liu et al., 2013). More than a thousand well preserved acanthomorphic acritarch specimens have also been observed in the NP section of Member III (Liu et al., 2013). The JLW and CJYZ cherts also display negative Ce anomalies (0.52–0.83), near seawater Y/Ho values (30–47), significant HREE depletion and low Al_2O_3 and TREE contents. These characteristics may reflect deeper water conditions compared to the BGY, NP and LHW sections. Abundant acritarch fossils have also been reported in the JLW and CJYZ

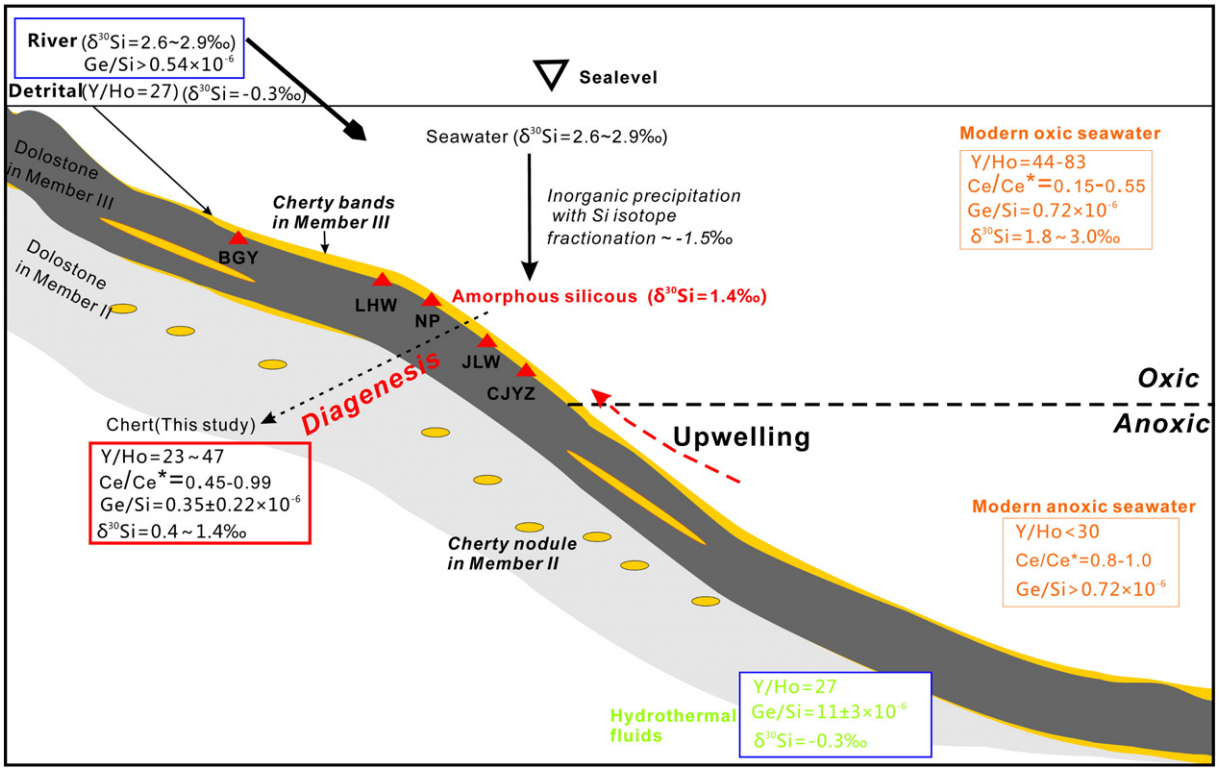

Fig. 7. Silica geochemical cycle model for the early Ediacaran Ocean and marine chemistry recorded by Member III of the Doushantuo Formation in Yangtze Three Gorges area, South China. The main Ge and Si sources in these cherts are dominated by seawater rather than hydrothermal fluids with minor continental detrital contribution in the shallow water BGY section. The dissolved silica is scavenged by inorganic precipitation as amorphous siliceous gel, which can result in light silica-enrichment in cherts given a stable fractionation of −1.5‰ (Geilert et al., 2014a). The kinetic fractionation during microquartz reprecipitation can explain the range of $\delta^{30}Si$ values, where parental carbonate was also altered during early diagenesis, forming chert nodules and bands. In oxic shallow water, dissolved Fe^{2+} and Mn^{2+} are oxidized into Fe and Mn-oxyhydroxide particles. Subsequently, the strong adsorption of Ge, Ho and Ce^{4+} by Fe- and Mn-oxyhydroxide particles would result in obvious negative Ce anomalies (0.15 ~ 0.55), decreased Ge/Si ratios (0.72×10^{-6}) and increased of Y/Ho ratios (up to 80) (Froelich et al., 1985; Bau et al., 1997; Nozaki et al., 1997). In anoxic deep water, the dissolution of Fe- and Mn-oxides could result in weak negative Ce anomalies, higher Ge/Si ratios and decreased of Y/Ho ratios (<30). The upwelling of anoxic deep water could also shift these proxies in the studied cherts.

cherts (McFadden et al., 2009; Liu et al., 2014). The JLW cherts from Member II recorded the rapid bacterial sulfate reduction (BSR) of highly metabolizable organic matter in a diagenetic environment with limited sulfate availability, ferruginous conditions and a low sedimentation rate (Xiao et al., 2010). In contrast, cherts from Member III exhibit near modern seawater Y/Ho ratios and negative Ce anomalies, indicating a stronger oxidization of dissolved Fe^{2+} and Mn^{2+} in Member III than Member II of the JLW section. The upper biozone (*H. scaberfacium* and *H. anozos*) began to bloom in the oxic seawater,.

5.6. Silica source and silicon isotope fractionation implications over time

The temporal chert $\delta^{30}Si$ value variations are plotted in Fig. 8. Robert and Chaussidon (2006) proposed that secular variations in Precambrian chert $\delta^{30}Si$ values are dependent on long-term ocean cooling, which was challenged by an alternative interpretation that attributed the diversity to a different silica source (van den Boorn et al., 2007, 2010). A number of studies have suggested that the bimodal distribution of $\delta^{30}Si$ values in Archean cherts reflect a mixing of two isotopically distinct fluids, as ^{30}Si-rich seawater and ^{30}Si-depleted hydrothermal fluids (van den Boorn et al., 2007, 2010; Abraham et al., 2011; Marin-Carbonne et al., 2012; Geilert et al., 2014b). This mixing model can explain the higher Ge/Si ratios and negative $\delta^{30}Si$ values in the Archean cherts (Hamade et al., 2003; van den Boorn et al., 2007, 2010; Marin-Carbonne et al., 2012). In addition, the continental weathering silica source in the Archean Ocean is limited on a large scale (André et al., 2006). Therefore, the positive $\delta^{30}Si$ values in the Archean cherts can be ascribed to removing ^{28}Si from seawater via Fe-oxide phase adsorption, the precipitation of authigenic clay minerals (Steinhoefel et al., 2009, 2010; Heck et al., 2011; Delvigne et al., 2012) and lower temperature fractionation during diagenesis (Stefurak et al., 2015). Recently, Stefurak et al. (2015) estimated the $\delta^{30}Si$ value of Archean seawater (~3.4 Ga) to be 1.6–2.6‰, corresponding with previous estimates (van den Boorn et al., 2007, 2010; Abraham et al., 2011).

Peritidal diagenetic cherts became widespread during the late Archean to Proterozoic. These diagenetic cherts often exhibit higher $\delta^{30}Si$ values than early Archean cherts (Fig. 8), such as 2.63-Ga Manjeri Formation cherts (1.56 ± 0.23‰) (Robert and Chaussidon, 2006), 2.53-Ga Griqualand West cherts, Transvaal SG., South Africa (1.84‰), 1.4–1.5 Ga Yusmastakh Formation cherts (1.20 ± 1.06‰) (Chakrabarti et al., 2012) and 1.88-Ga Gunflint cherts (1.56 ± 0.64‰) (Marin-Carbonne et al., 2012). The increasing $\delta^{30}Si$ trend in cherts from 3.8 to 1.5 Ga may reflect a gradual change from a hydrothermal to a continental weathering silica source (Heck et al., 2011; Delvigne et al., 2012; Chakrabarti et al., 2012). The $\delta^{30}Si$ values of these diagenetic cherts can be used to reconstruct seawater temperature and silicon isotopic compositions after carefully verifying certain criteria (Marin-Carbonne et al., 2012). The $\delta^{30}Si$ value of seawater was estimated to be 2 ± 1‰ in 1.88 Ga Gunflint cherts at a temperature (37–67 °C) (Marin-Carbonne et al., 2010), corresponding to a diagenetic chert with a $\delta^{30}Si$ value of 1 ± 1‰. The highest $\delta^{30}Si$ values are recorded in ca. 1.8 Ga cherts (Fig. 8), suggesting that dissolved silica concentrations reached a minimum level at that time.

The decreasing $\delta^{30}Si$ trend began in 1.5 Ga (Fig. 8) and may reflect a shift towards a continental weathering silica source. In this context, the co-precipitation of dissolved silica with Al phases could play an important role in the altering $\delta^{30}Si$ values in diagenetic cherts. Dissolution and reprecipitation during the early diagenetic processes could alter the $\delta^{30}Si$ values in microquartz (Marin-Carbonne et al., 2012, 2014). However, the whole rock samples may preserve the primary $\delta^{30}Si$ values of the original precursor sediments (Heck et al., 2011). In addition, Stefurak et al. (2015) suggested that the $\delta^{30}Si$ values of the early diagenetic white chert bands which were higher than that of the late stage black chert bands can be further inverted to estimate seawater $\delta^{30}Si$ values. If so, the highest $\delta^{30}Si$ values in our studied cherts represent a good approximation of low limit $\delta^{30}Si$ values of the seawater source condition, given that no other silica source existed (Marin-Carbonne et al., 2011). We assumed a silicon isotopic fractionation of −1.2‰ to −1.5‰ for the inorganic chemical precipitation of dissolved silica in seawater. Therefore, the $\delta^{30}Si$ values of Ediacaran seawater have been higher than 2.6‰ to 2.9‰ (Fig. 7). These high $\delta^{30}Si$ values are due to an enhancement in post-glaciation (Marinoan) weathering, when large silicon isotope fractionation resulted in high $\delta^{30}Si$ values in river influxes during the formation of secondary clay minerals (Ziegler et al., 2005; Opfergelt et al., 2010, 2012; Pogge von Strandmann et al., 2012).

6. Conclusions

Our study indicates that cherts (nodules and bands) in the Ediacaran Doushantuo Formation were formed by the replacement of carbonate during very early diagenesis and before compaction, in which amorphous siliceous gel precipitated from seawater/pore water and was converted to

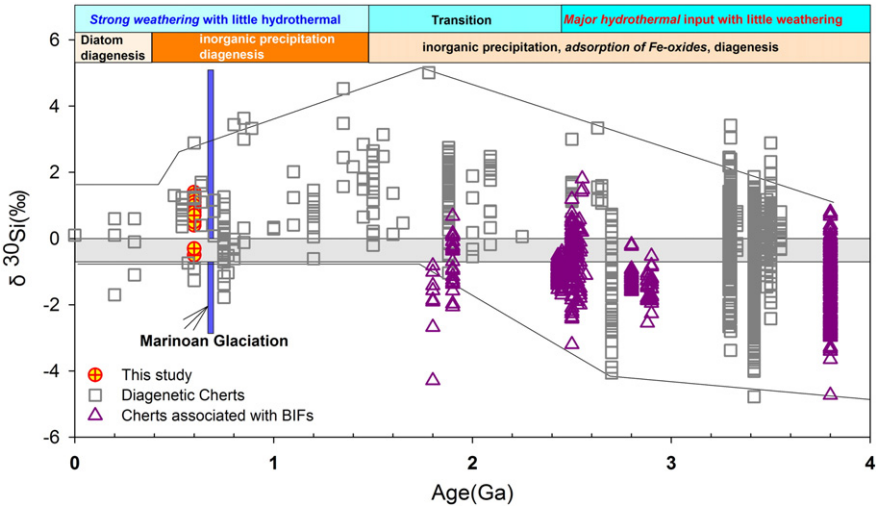

Fig. 8. The variations of $\delta^{30}Si$ values in diagenetic cherts and chert associated BIFs over time, indicate the silica source changes in the ocean from hydrothermal fluids to continental weathering and in a silicon isotope fractionation mechanism from inorganic precipitation to biotic adsorbing. The data includes available bulk rock and in situ MC–ICP-MS data as well as in situ ion-probe and SIMS data. These $\delta^{30}Si$ values of diagenetic cherts are cited from Robert and Chaussidon (2006), Abraham et al. (2011), Van den Boorn et al. (2010), Chakrabarti et al. (2012), Marin-Carbonne et al. (2012), Ramseyer et al. (2013), Hu et al. (2013), Geilert et al. (2014b) and Stefurak et al. (2015). These data of cherts associated with BIFs are referenced from André et al. (2006), Steinhoefel et al. (2009, 2010), Heck et al. (2011), Delvigne et al. (2012), Chakrabarti et al. (2012) and Li et al. (2014).

fibrous quartz and micro- and megaquartz by dissolution–recrystallization reactions. The dominant silica source in the Ediacaran Ocean is continental weathering rather than hydrothermal fluids. These cherts preserved primary chemical signals of the Ediacaran seawater, such as high $\delta^{30}Si$ values, negative Ce anomalies and HREE depletion. The negative Ce anomalies, REE + Y patterns and Ge/Si ratios in these cherts imply shallow oxic conditions during chert deposition in the Ediacaran Doushantuo Formation. This oxic environment could promote the evolution of acanthomorphic acritarcha from the lower biozone (*T. spinosa* assemblage) to the upper biozone (*H. scaberfacium* and *H. anozos*).

Acknowledgment

This project is funded by the National Basic Research Program of China (2014CB440906), the National Natural Science Foundation of China (41273024, 41573011), the Youth Innovation Promotion Association of the Chinese Academy of Sciences (2015), the CAS "Light of West China" Program (2014), and the 12th Five-Year Plan Project of the State Key Laboratory of Ore Deposit Geochemistry, CAS (SKLODG-ZY125-07). We thank Prof. Steve Barnes for improving the manuscript. We also thank all those who were responsible for reviewing the manuscript.

Appendix A

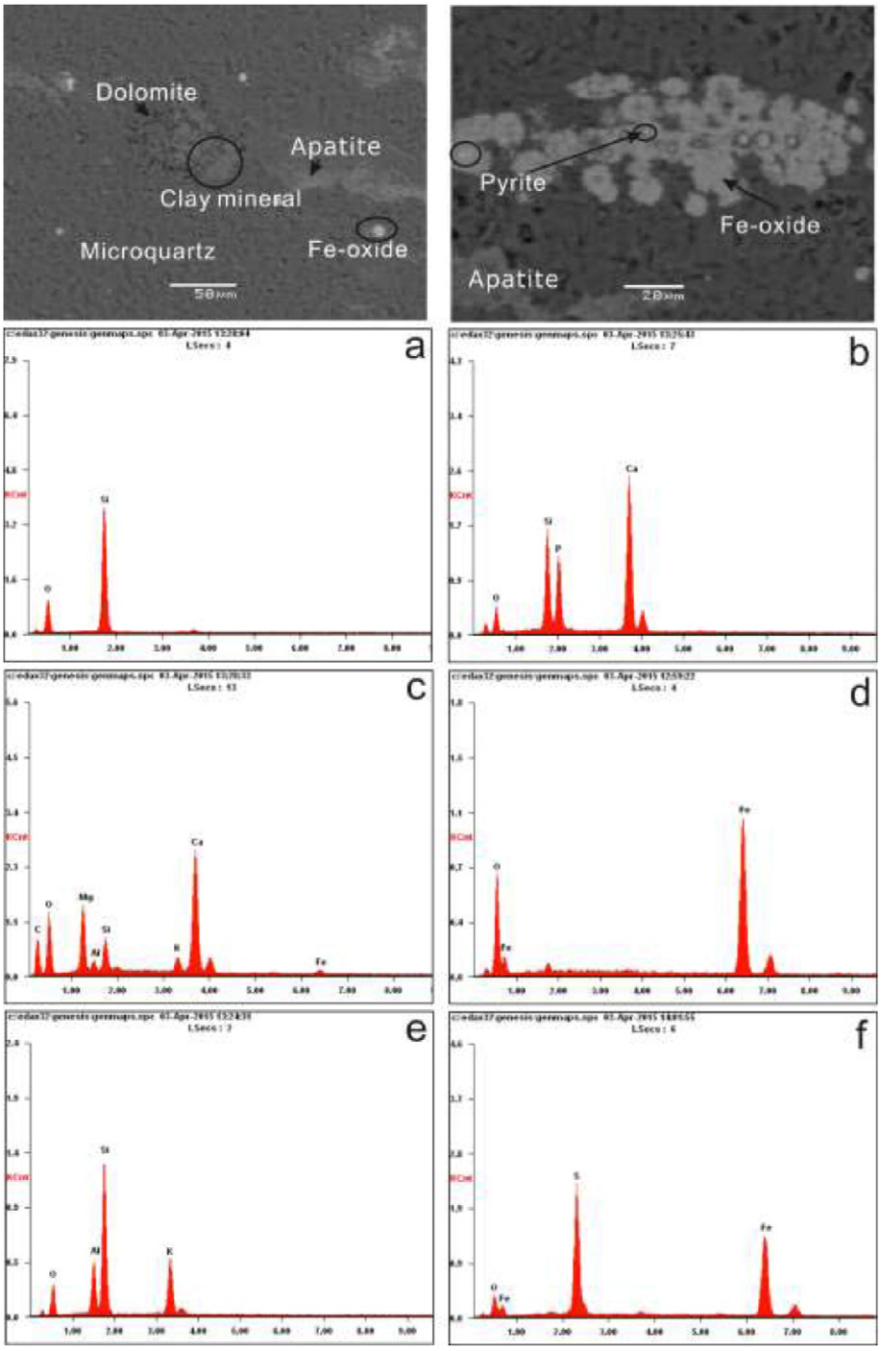

Appendix Fig. 1. SEM micrographs and the spectrum of the main minerals (quartz (a), apatite (b), dolomite (c), Fe-oxide (d) and clay minerals (e)) in cherts (BGY-4). Sometimes a little pyrite is observed as <20 μm in size, which was coated by Fe-oxides (f).

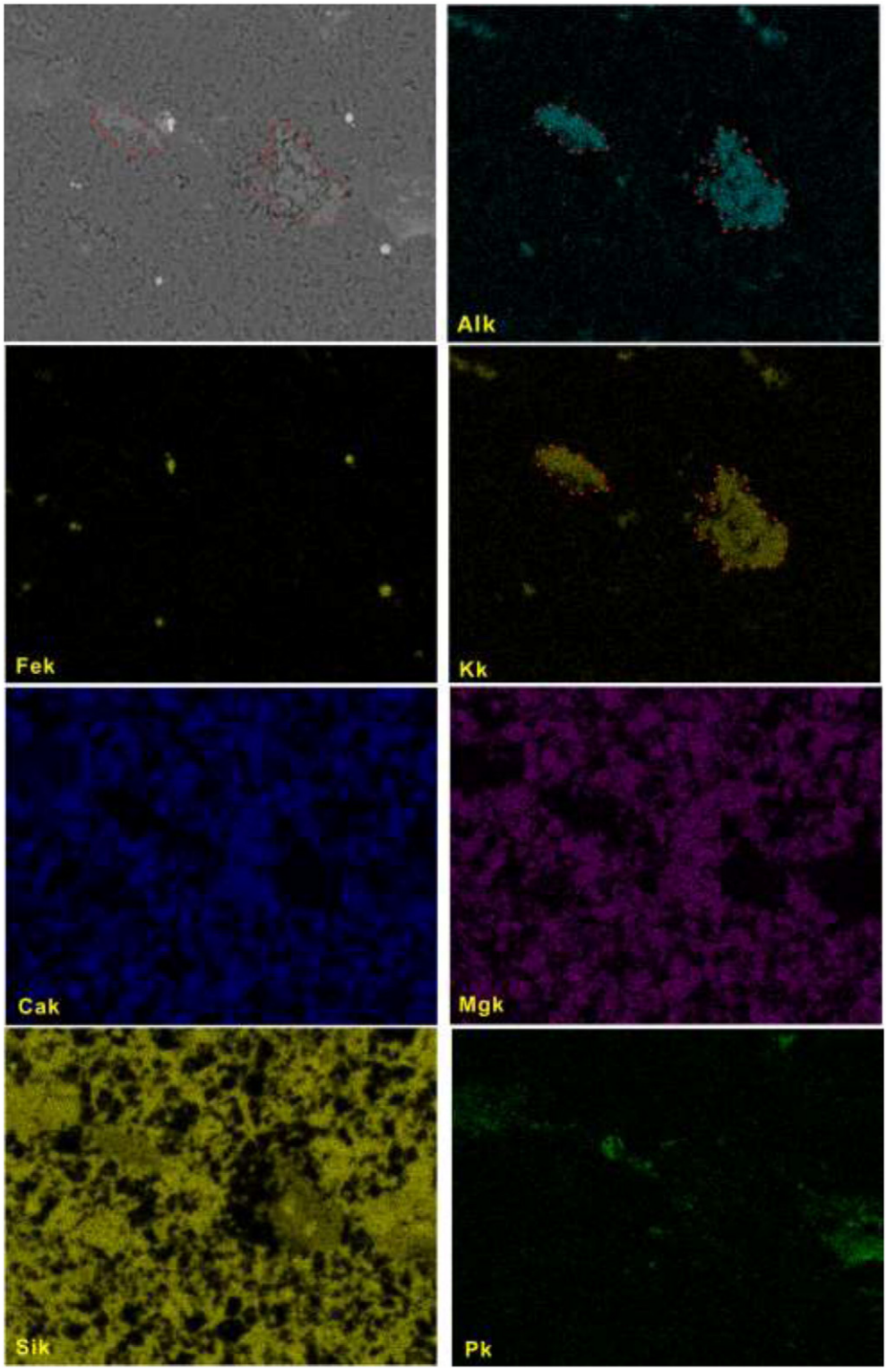

Appendix Fig. 2. The mapping of the major elements in BGY-4 chert by SEM micrograph. The chert contains more clay minerals, corresponding with high Al_2O_3 content. The homogeneous distribution of apatite minerals could indicate a shallow water oxic condition.

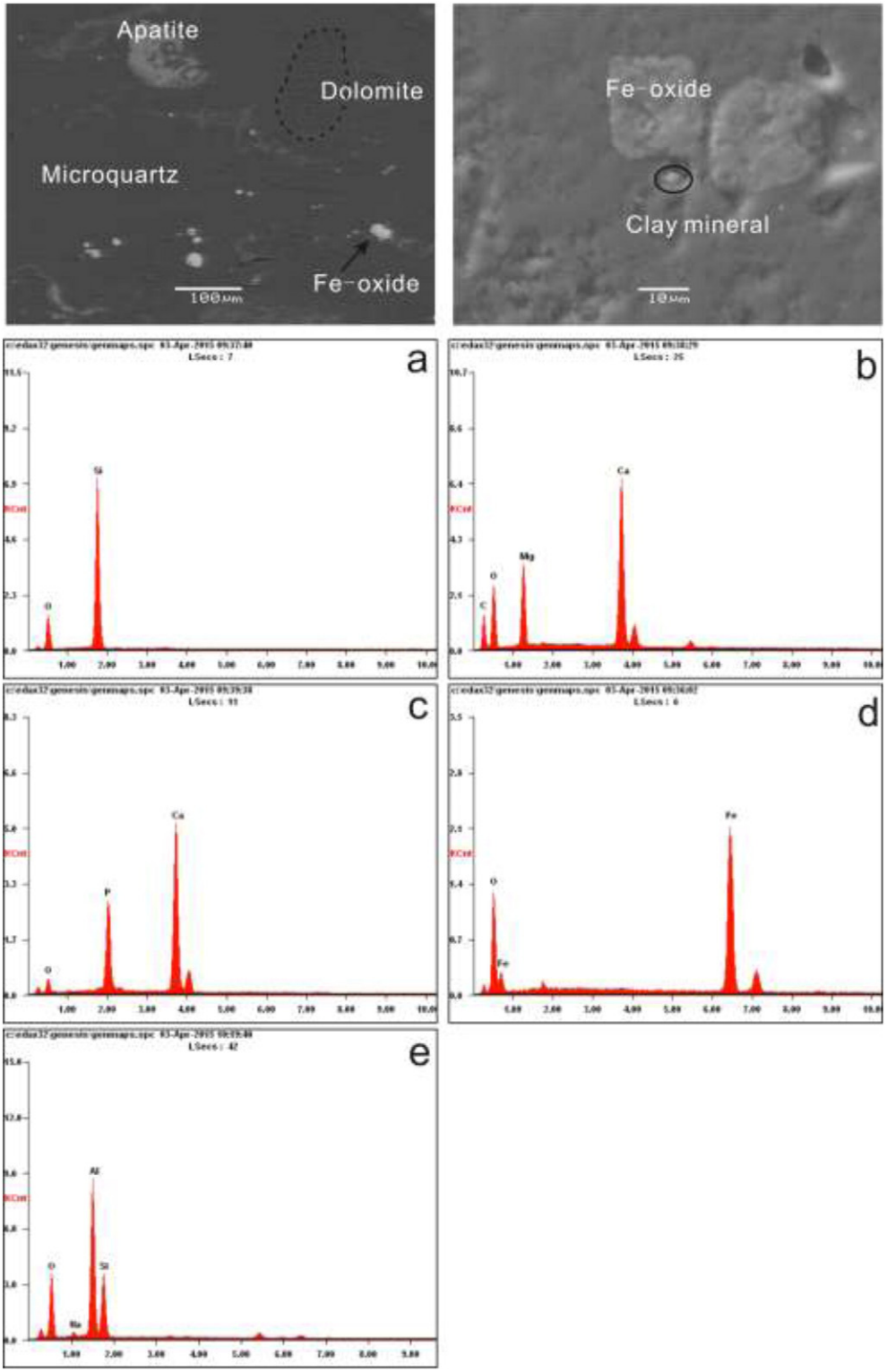

Appendix Fig. 3. SEM micrographs and the spectrum of the main minerals (quartz (a), dolomite (b), apatite (c), Fe-oxide (d) and clay minerals (e)) in LHW-13 cherts. A few clay minerals have been identified.

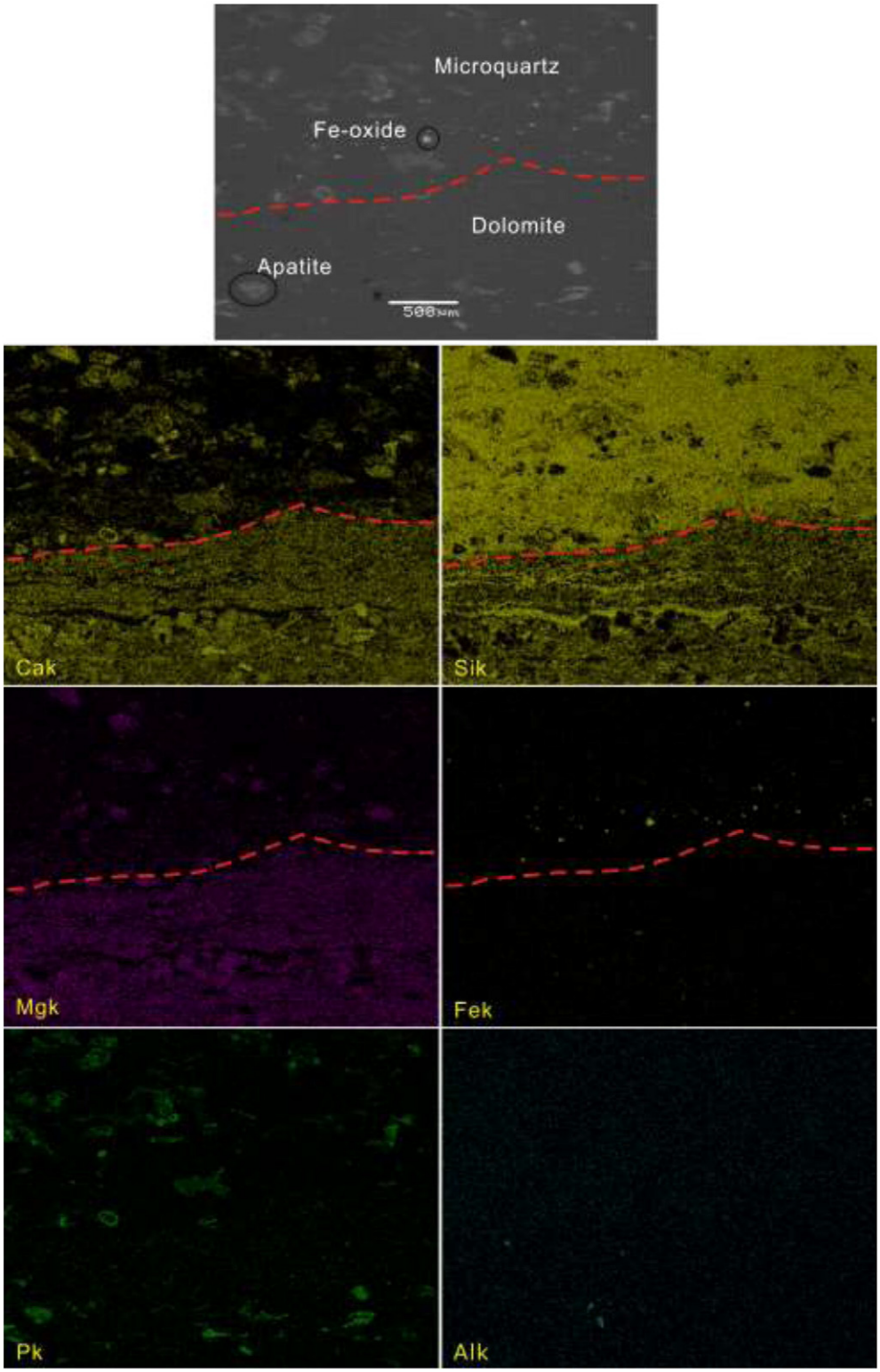

Appendix Fig. 4. SEM micrograph of the main mineral and the mapping of major elements distinctly show the boundary between dolostone and the chert matrix. The figure also suggests that parent carbonate and phosphate mineral have been altered by micro-quartz. Fe-oxides are present near the boundary between dolostone and the chert matrix. The homogeneous distribution of apatite minerals could also reflect a shallow water oxic condition.

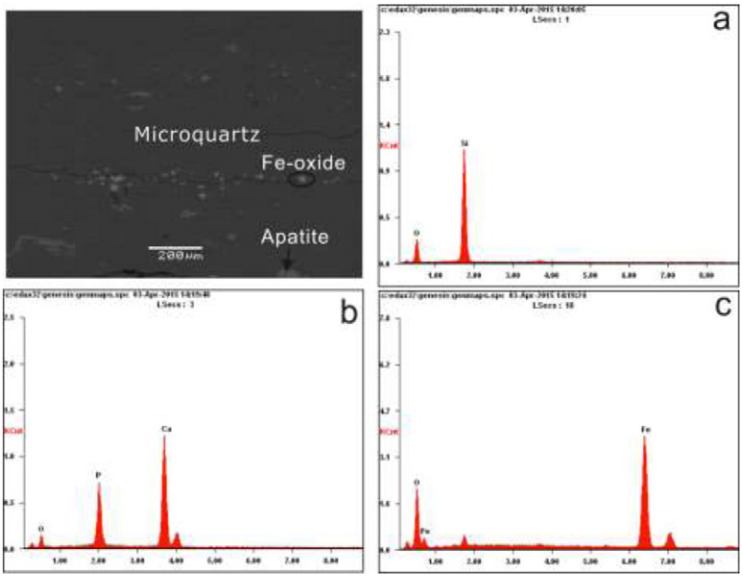

Appendix Fig. 5. SEM micrographs and the spectrum of the main minerals (quartz (a), apatite (b), Fe-oxide (c)) in NP-10 cherts. Fe-oxides often present near the boundary between dolostone and the chert matrix.

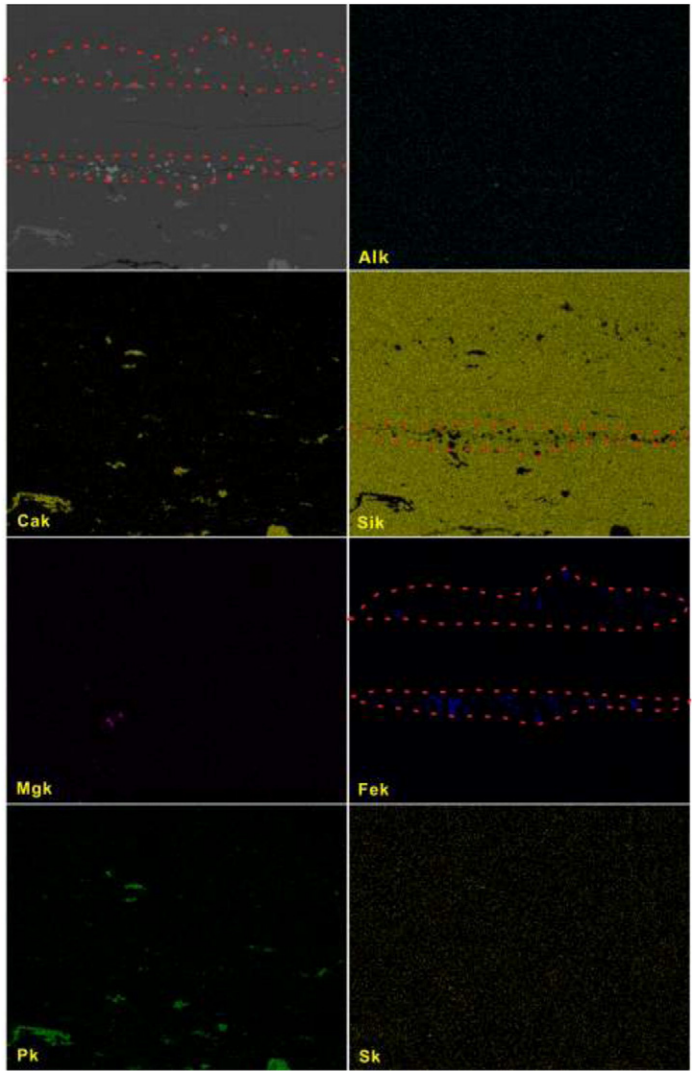

Appendix Fig. 6. SEM micrograph of the main mineral and the mapping of major elements distinctly show the boundary between dolostone and the chert matrix. Fe-oxides are commonly present in micro-quartz as a line.

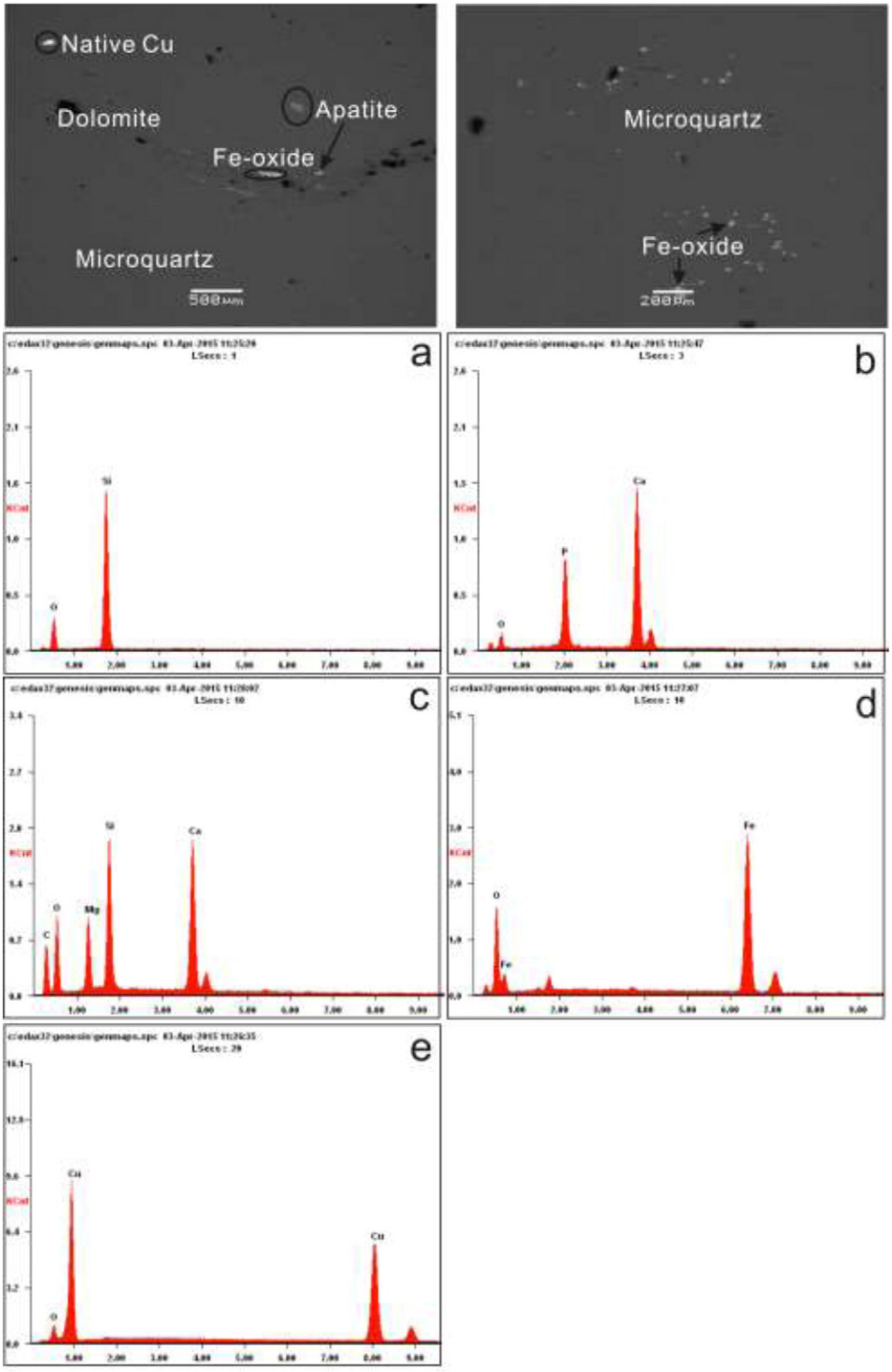

Appendix Fig. 7. SEM micrographs and the spectrum of the main minerals (quartz (a), apatite (b), dolomite (c), Fe-oxide (d)) in cherts (CJYZ-80). Sometimes a little native copper has been observed in cherts (e).

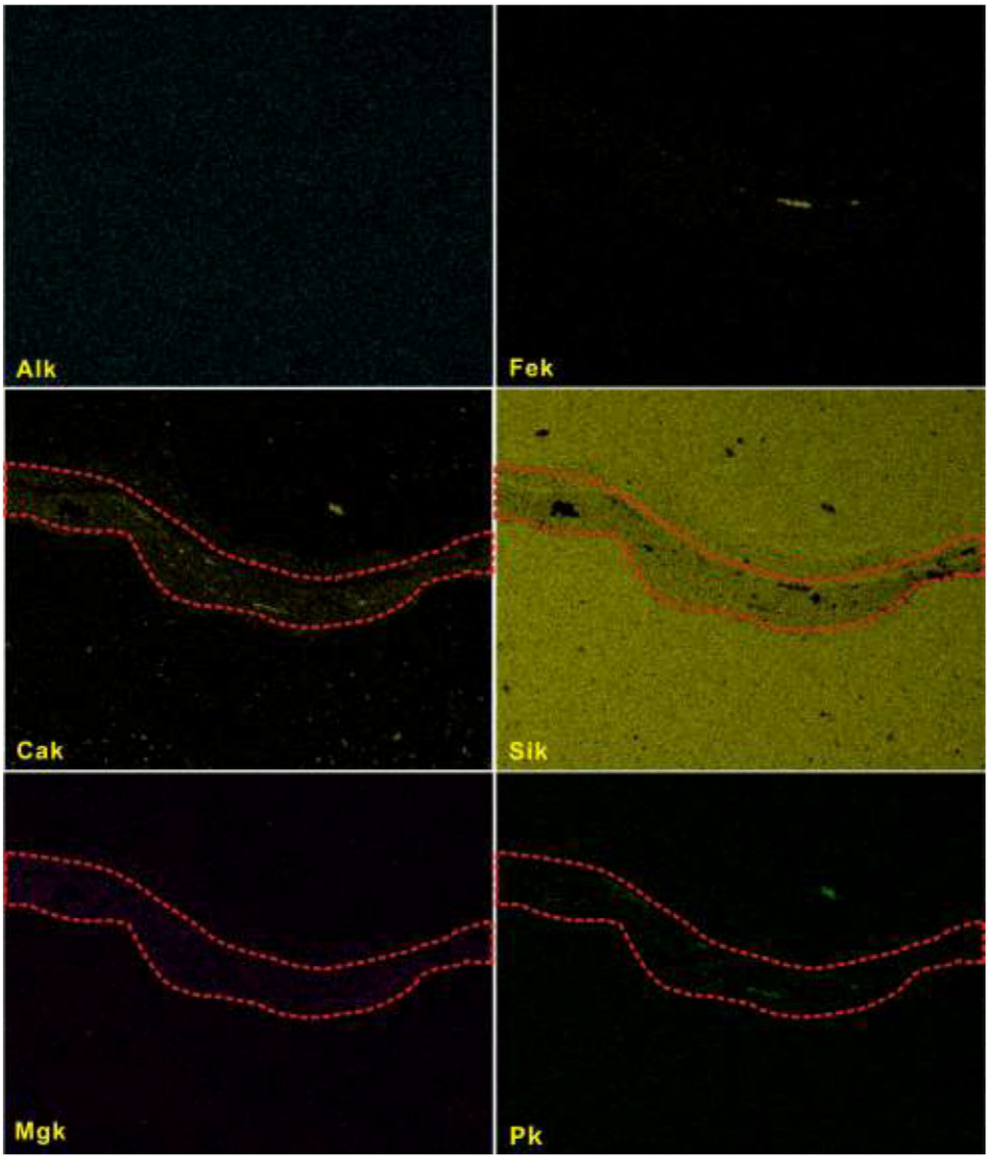

Appendix Fig. 8. The mapping of the major elements of the SEM micrograph in Appendix Fig. 7. The distinct boundary between dolostone and the chert matrix has also been observed. Fe-oxides are present at the boundary between dolomites and micro-quartz matrix.

LHW-24

[24 (2).xrdml] **Peak Search Report**

SCAN: 3.5131/69.9786/0.02626/17.34(sec), Cu(40kV,40mA), I(max)=12636, 04/03/15 11:19

PEAK: 17-pts/Parabolic Filter, Threshold=4.0, Cutoff=0.1%, BG=3/1.0, Peak-Top=Summit

NOTE: Intensity = Counts, 2T(0)=0.0(deg), Wavelength to Compute d-Spacing = 1.54056Å (Cu/K-alpha1)

#	2-Theta	d(Å)	BG	Height	Height%	Area	Area%	FWHM
1	6.242	14.1488	707	56	0.5	647	0.6	0.243
2	6.734	13.1162	734	45	0.4	816	0.8	0.381
3	7.188	12.2883	756	44	0.4	593	0.6	0.283
4	21.055	4.2159	386	2278	18.5	19224	18.5	0.188
5	22.422	3.9618	354	39	0.3	293	0.3	0.158
6	24.209	3.6733	336	74	0.6	950	0.9	0.270
7	26.833	3.3197	351	12285	100.0	103917	100.0	0.189
8	29.640	3.0114	306	277	2.3	3125	3.0	0.252
9	31.113	2.8722	295	556	4.5	7844	7.5	0.315
10	36.734	2.4446	243	712	5.8	7360	7.1	0.231
11	39.673	2.2700	217	814	6.6	7739	7.4	0.212
12	40.488	2.2261	224	313	2.5	2910	2.8	0.208
13	41.276	2.1854	218	141	1.1	1954	1.9	0.309
14	42.641	2.1186	199	498	4.1	4885	4.7	0.219
15	45.057	2.0104	184	78	0.6	1110	1.1	0.318
16	45.977	1.9723	184	336	2.7	3184	3.1	0.212
17	50.311	1.8121	201	1204	9.8	14256	13.7	0.264
18	55.038	1.6671	132	306	2.5	5967	5.7	0.435
19	55.508	1.6541	142	149	1.2	2111	2.0	0.316
20	60.130	1.5375	136	717	5.8	10087	9.7	0.314
21	64.176	1.4500	125	137	1.1	2179	2.1	0.355
22	67.879	1.3796	133	403	3.3	7518	7.2	0.416
23	68.324	1.3717	128	663	5.4	16889	16.3	0.569

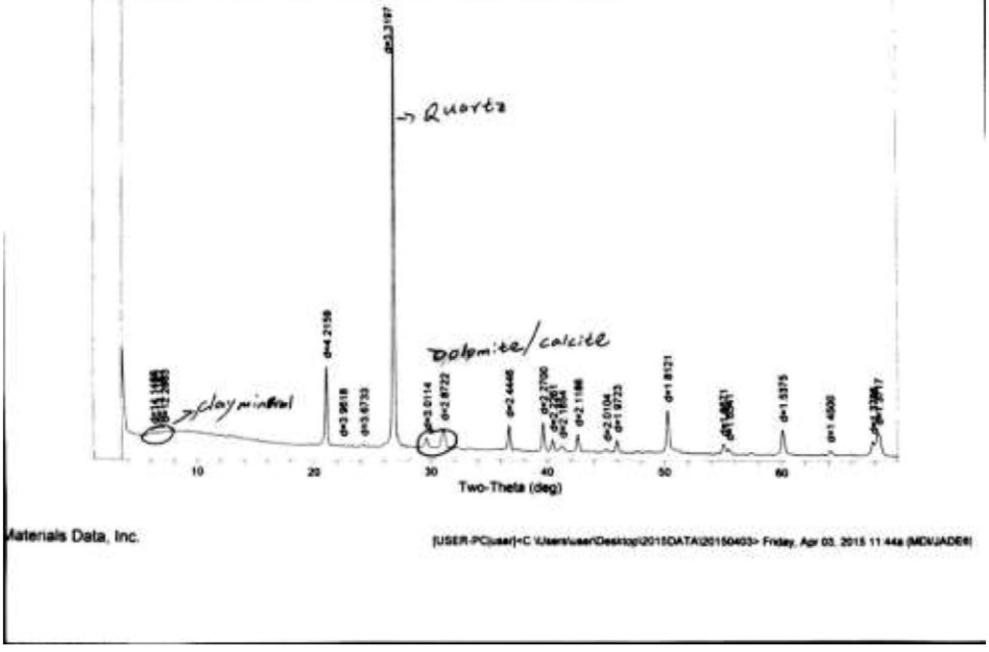

Materials Data, Inc.

[USER-PC\user]=C:\Users\user\Desktop\2015DATA\20150403> Friday, Apr 03, 2015 11:44a (MDI/JADE6)

Appendix Fig. 9. The XRD spectrum of the main minerals (quartz and dolomite/calcite) in LHW-24 chert. A few clay minerals have been identified.

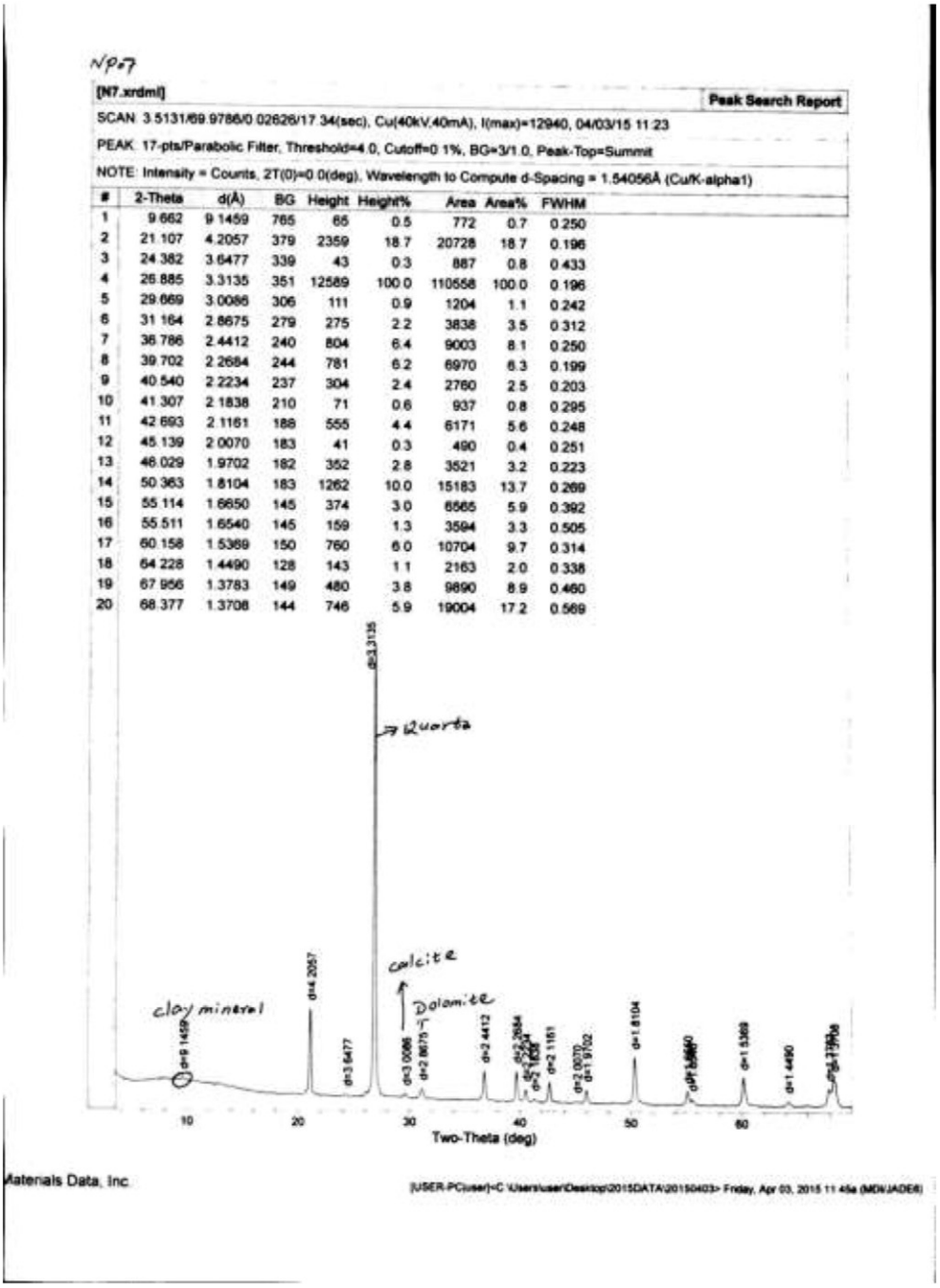

Appendix Fig. 10. The XRD spectrum of the main minerals (quartz and dolomite/calcite) in NP07 chert. A few clay minerals have been identified, which is consistent with SEM micrographs.

NP10

[N10.xrdml] **Peak Search Report**

SCAN: 3.5131/69.9786/0.02626/17.34(sec), Cu(40kV,40mA), I(max)=10930, 04/03/15 11:27

PEAK: 19-pts/Parabolic Filter, Threshold=4.0, Cutoff=0.1%, BG=3/1.0, Peak-Top=Summit

NOTE: Intensity = Counts, 2T(0)=0.0(deg), Wavelength to Compute d-Spacing = 1.54056Å (Cu/K-alpha1)

#	2-Theta	d(Å)	BG	Height	Height%	Area	Area%	FWHM
1	17.327	5.1137	419	41	0.4	400	0.4	0.205
2	21.054	4.2162	376	1822	17.2	17518	17.7	0.215
3	22.867	3.8858	346	16	0.2	32	0.0	0.100
4	24.207	3.6736	333	95	0.9	1650	1.7	0.388
5	26.832	3.3199	343	10587	100.0	99213	100.0	0.209
6	29.621	3.0134	299	68	0.6	685	0.7	0.212
7	31.113	2.8721	279	1003	9.5	12661	12.8	0.282
8	33.687	2.6584	245	58	0.5	677	0.7	0.245
9	36.733	2.4446	242	643	6.1	7180	7.2	0.249
10	37.497	2.3965	233	98	0.9	1117	1.1	0.254
11	39.672	2.2700	219	688	6.5	6898	7.0	0.224
12	40.488	2.2261	224	252	2.4	2560	2.6	0.227
13	41.302	2.1841	212	250	2.4	3156	3.2	0.282
14	42.640	2.1186	188	454	4.3	5439	5.5	0.267
15	45.109	2.0082	178	148	1.4	1825	1.8	0.275
16	45.977	1.9723	171	286	2.7	3267	3.3	0.255
17	50.310	1.8121	233	1034	9.8	13139	13.2	0.284
18	51.276	1.7802	247	49	0.5	-154	-0.2	0.026
19	55.036	1.6672	140	288	2.7	5136	5.2	0.398
20	55.482	1.6548	134	139	1.3	3567	3.6	0.573
21	60.105	1.5381	138	682	6.4	10526	10.6	0.345
22	64.202	1.4495	125	113	1.1	2511	2.5	0.496
23	67.879	1.3796	135	395	3.7	8726	8.8	0.493
24	68.324	1.3717	136	641	6.1	17654	17.8	0.615

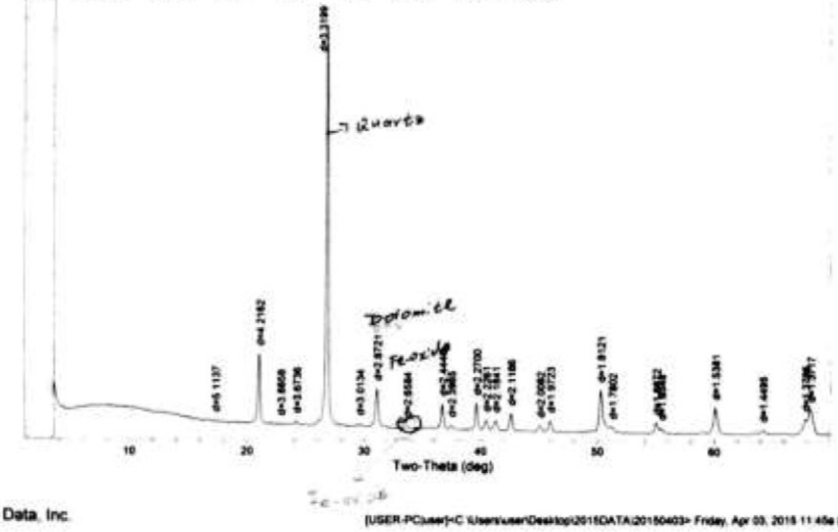

Materials Data, Inc.

[USER-PC\user]=C:\Users\user\Desktop\2015DATA\20150403> Friday, Apr 03, 2015 11:46a (MDI/JADE6)

Appendix Fig. 11. The XRD spectrum of the main minerals (quartz and dolomite/calcite) in NP10 chert. A few Fe-oxides have been identified.

Table 1
The $\delta^{30}Si$ values, major and trace elements content, and Ge/Si ratios of cherts in the studied five sections of Doushantuo Formation from Yangtze Gorges area, south China. SiO_2, Al_2O_3, Fe_2O_3 and P_2O_5 contents in BGY and LHW cherts were cited from Fan et al. (2014). Ge/Si ratios are reported as molar ratios following Shen et al. (2011).

Sample	Lithology	SiO_2 (%)	Al_2O_3 (%)	Fe_2O_3 (%)	CaO (%)	MgO (%)	P_2O_5 (%)	Zr (ppm)	Sc (ppm)	Ge (ppm)	Ge/Si (10^{-6})	$\delta^{30}Si$ (‰)	
Sampling site: Baiguoyuan section (BGY)													
BGY03	Chert	95.9	0.12	0.05	0.89	0.12	0.51	2.50	0.30	0.23	0.20	1.1	
BGY04	Chert	86.7	0.53	0.26	3.70	1.86	0.70	19.80	1.60	0.59	0.57	−0.5	
BGY05	Chert	95.5	0.31	0.10	0.86	0.11	0.53	8.20	1.00	0.71	0.62	−0.3	
BGY07	Chert	92.9	0.07	0.02	1.81	1.28	0.04	0.90	1.00	0.17	0.15	0.9	
BGY08	Chert	93.5	0.25	0.78	0.91	0.50	0.18	2.60	0.60	0.62	0.55	0.8	
Replication	Chert									0.62		0.9	
BGY10	Chert	94.8	0.15	0.14	1.16	0.86	0.07	2.60	0.50	0.28	0.25	1	
BGY13	Chert	82.0	0.13	0.05	5.17	3.37	0.03	1.70	0.70	0.31	0.32	0.9	
Sampling site: Liuhuiwan section (LHW)													
LHW02	Chert	92.2	0.17	0.07	2.16	0.90	0.64	1.90	0.50	0.31	0.28	1.4	
LHW03	Chert	75.1	0.19	0.05	7.18	4.86	0.17	2.30	0.70	0.17	0.19	1.2	
LHW04	Chert	93.9	0.15	0.06	1.49	0.60	0.42	2.90	0.40	0.23	0.20	1	
LHW05	Chert	86.9	0.26	0.08	3.52	2.21	0.22	3.80	1.10	0.30	0.29	0.4	
LHW07	Chert	84.0	0.17	0.10	4.56	2.67	0.48	2.20	0.70	0.32	0.32	1.2	
LHW09	Chert	77.3	0.22	0.12	7.39	3.49	1.60	3.00	0.50	0.36	0.39	1.3	
LHW10	Chert	86.3	0.18	0.07	3.92	2.20	0.58	3.10	0.50	0.56	0.54	1.2	
LHW13	Chert	87.9	0.07	0.01	3.24	2.20	0.10	0.60	0.00	0.09	0.09	0.5	
LHW14	Chert	92.8	0.08	0.01	1.59	1.16	0.06	0.50	0.00	0.10	0.09	0.9	
LHW23	Chert	67.9	0.33	0.45	10.08	5.56	0.11	3.80	0.70	0.36	0.44	1.1	
LHW24	Chert	77.5	0.33	0.14	7.21	3.45	0.58	3.30	0.60	0.47	0.51	0.9	
LHW25	Chert	80.6	0.19	0.18	6.31	2.87	0.40	4.30	0.30	0.33	0.34	1.1	
LHW26	Chert	84.5	0.15	0.03	4.91	2.07	0.68	2.10	0.70	0.20	0.20	1	
Sampling site: Niuping section (NP)													
NP01	Chert	84.5	0.21	0.17	4.24	3.62	0.06	2.30	2.70	0.27	0.26	0.4	
NP02	Chert	92.8	0.26	0.20	1.66	1.46	0.03	4.00	1.00	0.59	0.53	0.5	
NP03	Chert	81.6	0.25	0.11	5.06	4.58	0.03	2.00	3.50	0.65	0.67	1	
NP04	Chert	96.7	0.15	0.12	0.97	0.40	0.04	3.20	0.50	0.45	0.39	0.8	
NP05	Chert	94.9	0.23	0.11	0.77	2.30	0.04	1.80	0.40	0.77	0.67	0.7	
NP06	Chert	76.1	0.44	0.35	6.63	5.18	0.07	5.20	3.90	0.32	0.35	0.9	
NP07	Chert	87.7	0.55	0.20	2.70	3.44	0.12	5.70	1.60	0.66	0.62	1	
NP08	Chert	67.3	0.50	1.15	9.80	5.62	0.14	5.40	6.50	0.60	0.74	0.8	
NP09	Chert	81.3	0.37	0.84	4.62	4.01	0.07	4.30	3.20	0.53	0.54	0.7	
NP10	Chert	79.2	0.22	0.16	6.14	4.05	0.05	3.00	4.30	0.91	0.95	0.7	
Sampling site: Jiulongwan section (JLW)													
JLW32	Chert	76.3	0.12	0.12	7.30	4.58	0.02	1.90	0.63	0.6	0.69		
JLW33	Chert	80.1	0.09	0.30	6.44	3.31	0.01	0.70	0.36	0.4	0.38		
JLW34	Chert	95.0	0.35	0.21	1.24	0.07	0.14	5.10	0.82	0.8	0.72		
JLW35	Chert	93.5	0.18	0.15	2.17	0.35	0.42	3.10	0.56	0.6	0.50		
JLW36	Chert	95.6	0.18	0.08	1.09	0.30	0.02	2.40	0.36	0.4	0.32		
JLW38	Chert	80.8	0.10	0.26	5.68	3.52	0.02	1.40	0.36	0.4	0.37		
JLW39	Chert	91.0	0.11	0.09	3.26	0.85	0.01	1.00	0.22	0.2	0.20		
Sampling site: Chenjiayuanzi section (CJYZ)													
CJYZ-15	Chert	95.4	0.02	0.01	0.48	0.05	0.21	1.20	<0.1	0.13	0.11		
CJYZ-17	Chert	92.0	0.15	0.07	1.96	0.71	0.55	2.10	0.20	0.17	0.15		
CJYZ-19	Chert	92.9	0.19	0.11	2.11	1.11	0.11	3.10	0.30	0.15	0.13		
CJYZ-32	Chert	88.6	0.11	0.26	3.68	2.12	0.12	2.10	0.10	0.1	0.09		
CJYZ-35	Chert	96.8	0.15	0.07	0.53	0.05	0.16	1.90	0.10	0.05	0.04		
CJYZ-38	Chert	97.1	0.08	0.03	0.46	0.27	0.02	0.80	0.10	0.13	0.11		
CJYZ-40	Chert	96.1	0.08	0.06	0.77	0.46	0.04	1.50	0.10	0.15	0.13		
CJYZ-80	Chert	97.7	0.08	0.03	0.34	0.15	0.02	0.60	<0.1	0.11	0.09		
CJYZ-81	Chert	96.2	0.11	0.10	0.87	0.03	0.08	<0.5	<0.1	0.07	0.06		
Reference materials													
SARM-45	Cement	50.1	26.3	12.72	0.77	3.47	0.08						This study
Reference value		49.6	26.22	12.60	0.78	3.39	0.08						
AMH-1	Andesite							146.75 ± 3.69	13.65 ± 0.80	1.21 ± 0.11			This study
Reference value								139–149	13.2–15	1.1			http://georem.mpch-mainz.gwdg.de/sample_query.asp
AGV-2	Andesite							237 ± 10	13.8 ± 0.5	1.24 ± 0.11		−0.1	This study
Reference value								230	13	1.11–1.43		−0.13 ± 0.16	Geilert et al. (2014a, 2014b), http://georem.mpch-mainz.gwdg.de/sample_query.asp
Reference value												−0.14 ± 0.05	Zambardi and Poitrasson (2010)
Reference value												−0.21 ± 0.07	Savage et al. (2011)

Table 2
The rare earth element contents in cherts and interlaminated dolostones from the studied five sections. Total rare earth elements (TREE) contents are the sum of all rare earth elements and Y contents. Ce/Ce* = CeN / (2PrN − NdN), Eu/Eu* = EuN / (0.67SmN + 0.33TbN).

Samples Reference matierals	Lithilogy	La (ppm)	Ce (ppm)	Pr (ppm)	Nd (ppm)	Sm (ppm)	Eu (ppm)	Gd (ppm)
AMH-1	Andesite	17.55 ± 0.44	36.76 ± 1.18	4.41 ± 0.11	17.70 ± 0.53	3.54 ± 0.25	1.18 ± 0.07	3.24 ± 0.13
Reference	http://georem.mpch-mainz.gwdg.de/sample_query.asp	15.69–16.9	33.03–35.1	4.037–4.51	16.61–18.1	3.66–3.91	1.04–1.21	3.09–3.68
AGV-2	Andesite	38.6 ± 1.4	69.5 ± 2.7	8.02 ± 0.26	30.4 ± 1.1	5.47 ± 0.19	1.55 ± 0.08	4.64 ± 0.27
Reference	Raczek et al., 2001;http://georem.mpch-mainz.gwdg.de/sample_query.asp	37.9	68.6	7.84	30.5	5.49	1.53	4.52
Sampling site: *Baiguoyuan section*								
BGY03	Chert	3.14	3.83	0.75	3.47	0.57	0.16	0.71
BGY04	Chert	13.5	15.5	3.6	16.1	2.93	0.68	2.74
BGY05	Chert	11.7	11.7	2.41	10	1.7	0.39	1.61
BGY07	Chert	0.63	0.74	0.14	0.59	0.1	0.03	0.14
BGY08	Chert	1.67	2.42	0.55	2.48	0.4	0.1	0.4
BGY10	Chert	1.18	1.67	0.35	1.57	0.29	0.06	0.29
BGY13	Chert	1.2	1.69	0.32	1.36	0.25	0.06	0.31
BGY06	Dolostone	4.83	6.45	1.16	5.06	0.93	0.23	1.04
BGY09	Dolostone	5.4	7.07	1.23	5.03	0.94	0.21	0.95
BGY12	Dolostone	3.51	4.57	0.73	3.03	0.53	0.15	0.57
Sampling site: Liuhuiwan section								
LHW02	Chert	3.1	6.1	0.72	3.06	0.56	0.15	0.62
LHW03	Chert	1.06	1.92	0.23	0.86	0.21	0.04	0.22
LHW04	Chert	2.09	3.79	0.43	1.75	0.34	0.09	0.41
LHW05	Chert	1.4	2.31	0.29	1.23	0.27	0.06	0.28
LHW07	Chert	1.36	2.46	0.31	1.31	0.27	0.06	0.27
LHW09	Chert	3.01	4.8	0.53	2.28	0.43	0.12	0.51
LHW10	Chert	2.71	4.17	0.59	2.46	0.49	0.12	0.53
LHW13	Chert	0.21	0.32	0.05	0.17	0.05	0.02	0.03
LHW14	Chert	0.15	0.22	0.03	0.12	0.02	0.01	0.03
LHW23	Chert	2.16	3.98	0.55	2.37	0.42	0.1	0.52
LHW24	Chert	3.08	5.57	0.76	3.56	0.71	0.17	0.79
LHW25	Chert	2.3	3.98	0.54	2.3	0.46	0.12	0.51
LHW26	Chert	3.14	4.31	0.66	2.55	0.43	0.11	0.52
LHW06	Dolostone	4.81	8.35	1.11	4.59	0.92	0.22	0.95
LHW11	Dolostone	0.36	0.65	0.08	0.33	0.07	0.01	0.08
LHW22	Dolostone	1.98	3.3	0.4	1.64	0.34	0.08	0.36
Sampling site: Niuping section								
NP01	Chert	1.14	1.86	0.34	1.51	0.34	0.06	0.23
NP02	Chert	1.28	2.45	0.42	1.97	0.5	0.12	0.47
NP03	Chert	1.44	2.01	0.4	1.55	0.22	0.06	0.26
NP04	Chert	0.99	1.5	0.29	1.34	0.23	0.06	0.27
NP05	Chert	0.82	1.44	0.28	1.31	0.23	0.05	0.22
NP06	Chert	3.13	4.07	0.98	4.45	0.82	0.18	0.76
NP07	Chert	3.69	4.46	1.07	4.46	0.86	0.21	0.88
NP08	Chert	2.03	2.73	0.47	1.92	0.35	0.1	0.44
NP09	Chert	2.62	3.76	0.73	3.32	0.73	0.16	0.66
NP10	Chert	2.05	2.63	0.56	2.58	0.43	0.1	0.45
NP11	Dolostone	2.15	2.86	0.51	2.37	0.5	0.16	0.56
Sampling site: Jiulongwan section								
JLW32	Chert	2	2.98	0.44	1.83	0.31	0.11	0.28
JLW33	Chert	1.38	2.01	0.28	1.03	0.18	0.05	0.15
JLW34	Chert	2.93	4.9	0.82	3.53	0.57	0.13	0.55
JLW35	Chert	5.8	9.33	1.43	6.08	0.95	0.22	0.93
JLW36	Chert	0.39	0.62	0.09	0.36	0.07	0.01	0.05
JLW38	Chert	1.89	2.43	0.4	1.57	0.27	0.06	0.19
JLW39	Chert	1.55	1.78	0.29	1.11	0.13	0.04	0.15
JLW37	Dolostone	7.9	12	1.64	6.37	1.19	0.27	1.11
JLW41	Dolostone	4	5.55	0.88	3.6	0.67	0.14	0.57
Sampling site: Chenjiayuanzi section								
CJYZ-15	Chert	0.8	1.13	0.2	0.9	0.17	0.04	0.18
CJYZ-17	Chert	4.3	5.59	0.8	3.2	0.6	0.15	0.6
CJYZ-19	Chert	1.5	2.56	0.43	1.8	0.34	0.08	0.35
CJYZ-32	Chert	0.8	1.28	0.19	0.8	0.14	0.04	0.14
CJYZ-35	Chert	2	2.73	0.53	2.4	0.4	0.09	0.34
CJYZ-38	Chert	<0.5	0.55	0.11	0.5	0.08	<0.03	0.07
CJYZ-40	Chert	0.7	0.9	0.2	1	0.19	<0.03	0.14
CJYZ-80	Chert	<0.5	0.49	0.08	0.4	0.08	<0.03	0.06
CJYZ-81	Chert	0.8	1.07	0.23	1	0.19	0.04	0.16
CJYZ-16	Dolostone	3	4.36	0.62	2.5	0.46	0.12	0.44
CJYZ-39	Dolostone	5	6.12	1.09	4.5	0.78	0.17	0.62

Tb (ppm)	Dy (ppm)	Y (ppm)	Ho (ppm)	Er (ppm)	Tm (ppm)	Yb (ppm)	Lu (ppm)	TREE (ppm)	Y/Ho	Ce/Ce*
0.53 ± 0.03	2.74 ± 0.10	15.36 ± 0.73	0.55 ± 0.03	1.53 ± 0.08	0.21 ± 0.02	1.37 ± 0.10	0.203 ± 0.01			
0.5–0.53	2.75–3	16.44	0.55–0.59	1.52–1.58	0.21–0.23	1.35–1.45	0.19–0.23			
0.67 ± 0.03	3.37 ± 0.10	19 ± 0.7	0.67 ± 0.03	1.86 ± 0.07	0.26 ± 0.01	1.62 ± 0.08	0.249 ± 0.018			
0.64	3.47	20	0.653	1.81	0.259	1.62	0.247			
0.08	0.45	3.02	0.1	0.26	0.03	0.15	0.02	16.74	29	0.62
0.37	1.89	11.7	0.41	1.1	0.14	0.89	0.13	71.67	29	0.5
0.23	1.21	8.81	0.28	0.78	0.09	0.58	0.09	51.57	32	0.52
0.02	0.08	0.65	0.02	0.06	0.01	0.04	0.01	3.25	30	0.59
0.06	0.3	1.46	0.06	0.15	0.01	0.1	0.01	10.18	26	0.51
0.04	0.16	0.93	0.04	0.09	0.01	0.1	0.01	6.79	25	0.56
0.03	0.22	1.07	0.05	0.11	0.01	0.11	0.01	6.8	23	0.58
0.16	0.91	6.22	0.21	0.6	0.08	0.54	0.09	28.5	29	0.63
0.14	0.84	4.6	0.18	0.49	0.07	0.42	0.07	27.62	26	0.61
0.09	0.41	2.53	0.1	0.23	0.03	0.18	0.02	16.69	25	0.68
0.11	0.49	3.71	0.11	0.3	0.03	0.15	0.02	19.21	33	0.95
0.04	0.19	1.42	0.04	0.12	0.01	0.09	0.01	6.46	33	0.82
0.06	0.36	2.81	0.08	0.23	0.03	0.17	0.02	12.65	33	0.95
0.05	0.24	1.85	0.06	0.17	0.02	0.12	0.02	8.38	29	0.86
0.05	0.29	2.29	0.06	0.19	0.02	0.11	0.02	9.08	40	0.85
0.08	0.47	3.52	0.11	0.26	0.03	0.2	0.03	16.38	32	1
0.08	0.5	3.91	0.11	0.29	0.04	0.26	0.03	16.28	36	0.77
0.01	0.04	0.31	0.01	0.02	0	0.02	0	1.26	23	0.65
0	0.02	0.22	0.01	0.02	0	0.01	0	0.86	32	0.87
0.08	0.46	2.32	0.09	0.22	0.03	0.18	0.03	13.52	27	0.82
0.12	0.63	3.9	0.15	0.37	0.05	0.3	0.04	20.2	26	0.89
0.08	0.41	2.82	0.11	0.23	0.04	0.24	0.03	14.17	27	0.82
0.07	0.36	2.86	0.09	0.22	0.03	0.15	0.03	15.52	32	0.66
0.15	0.8	5.35	0.2	0.44	0.07	0.39	0.05	28.4	26	0.81
0.01	0.09	0.44	0.02	0.05	0	0.04	0.01	2.23	29	0.87
0.05	0.28	1.68	0.07	0.2	0.03	0.16	0.02	10.59	25	0.86
0.04	0.22	1.42	0.04	0.1	0.01	0.06	0.01	7.38	36	0.64
0.06	0.34	2.1	0.06	0.16	0.02	0.11	0.01	10.07	35	0.73
0.04	0.21	1.68	0.04	0.12	0.02	0.08	0.01	8.14	39	0.51
0.03	0.18	1.31	0.03	0.08	0.02	0.07	0.01	6.41	39	0.63
0.03	0.15	1.2	0.04	0.1	0.01	0.09	0.01	5.98	31	0.64
0.1	0.47	3.1	0.08	0.25	0.03	0.15	0.02	18.57	40	0.49
0.11	0.56	4.05	0.12	0.26	0.03	0.16	0.03	20.94	35	0.45
0.07	0.36	3.06	0.07	0.19	0.02	0.15	0.02	11.99	42	0.62
0.1	0.46	2.98	0.09	0.23	0.02	0.16	0.02	16.04	32	0.61
0.07	0.28	1.93	0.05	0.14	0.02	0.11	0.01	11.4	43	0.58
0.08	0.45	3.99	0.1	0.25	0.03	0.15	0.02	14.19	40	0.67
0.04	0.2	1.99	0.05	0.12	0.01	0.1	0.02	10.49	42	0.74
0.02	0.09	0.86	0.02	0.06	0	0.04	0	6.18	45	0.68
0.08	0.39	2.81	0.07	0.17	0.02	0.11	0.02	17.1	39	0.67
0.13	0.56	5.03	0.12	0.24	0.03	0.12	0.02	30.98	43	0.72
0.01	0.06	0.65	0.01	0.05	0.01	0.04	0.01	2.41	44	0.78
0.04	0.18	1.51	0.04	0.08	0.01	0.08	0.01	8.76	37	0.61
0.02	0.09	0.69	0.02	0.04	0	0.02	0	5.94	33	0.62
0.17	0.96	8.81	0.22	0.62	0.1	0.53	0.08	41.95	41	0.74
0.08	0.38	3.37	0.08	0.24	0.03	0.15	0.02	19.75	40	0.67
0.02	0.14	1.4	0.03	0.08	0.01	0.06	0.01	5.17	47	0.66
0.08	0.48	4.6	0.11	0.27	0.03	0.16	0.02	20.99	42	0.73
0.05	0.31	3	0.07	0.2	0.03	0.16	0.03	10.91	43	0.65
0.02	0.11	0.8	0.02	0.05	0.01	0.04	0.01	4.45	40	0.73
0.04	0.18	1.2	0.04	0.07	0.01	0.05	0.01	10.09	30	0.61
0.01	<0.05	0.3	0.01	<0.03	<0.01	<0.03	0.01	1.64	30	0.59
0.02	0.09	0.6	0.02	0.05	0.01	0.13	0.05	4.1	30	0.61
0.01	<0.05	0.3	0.01	<0.03	<0.01	<0.03	<0.01	1.43	30	0.83
0.02	0.09	0.6	0.02	0.04	<0.01	<0.03	<0.01	4.26	30	0.52
0.07	0.41	3.6	0.1	0.29	0.04	0.28	0.05	16.34	36	0.74
0.09	0.44	3.1	0.09	0.24	0.03	0.16	0.03	22.46	34	0.6

References

Abraham, K., Hofmann, A., Foley, S.F., Cardinal, D., Harris, C., Barth, M.G., André, L., 2011. Coupled silicon–oxygen isotope fractionation traces Archaean silicification. Earth Planet. Sci. Lett. 301, 222–230.

Alibo, D.S., Nozaki, Y., 1999. Rare earth elements in seawater: particle association, shale-normalization, and Ce oxidation. Geochim. Cosmochim. Acta 63, 363–372.

André, L., Cardinal, D., Alleman, L.Y., Moorbath, S., 2006. Silicon isotopes in 3.8 Ga West Greenland rocks as clues to the Eoarchaean supracrustal Si cycle. Earth Planet. Sci. Lett. 245, 162–173.

Basile-Doelsch, I., Meunier, J., Parron, C., 2005. Another continental pool in the terrestrial silicon cycle. Nature 433, 399–402.

Bau, M., Dulski, P., 1999. Comparing yttrium and rare earths in hydrothermal fluids from the Mid-Atlantic Ridge: implications for Y and REE behaviour during near-vent mixing and for the YrHo ratio of Proterozoic seawater. Chem. Geol. 155, 77–90.

Bau, M., Koschinsky, A., Dulski, P., Hein, J.R., 1996. Comparison of the partitioning behaviours of yttrium, rare earth elements, and titanium between hydrogenetic marine ferromanganese crusts and seawater. Geochim. Cosmochim. Acta 60, 1709–1725.

Bau, M., Möller, P., Dulski, P., 1997. Yttrium and lanthanides in eastern Mediterranean seawater and their fractionation during redox-cycling. Mar. Chem. 56, 123–131.

Chakrabarti, R., Knoll, A.H., Jacobsen, S.B., Fischer, W.W., 2012. Si isotope variability in Proterozoic cherts. Geochim. Cosmochim. Acta 91, 187–201.

Condon, D., Zhu, M., Bowring, S., Wang, W., Yang, A., Jin, Y., 2005. U–Pb ages from the neoproterozoic Doushantuo Formation, China. Science 308, 95–98.

Delstanche, S., Opfergelt, S., Cardinal, D., Elsass, F., André, L., Delvaux, B., 2009. Silicon isotopic fractionation during adsorption of aqueous monosilicic acid onto iron oxide. Geochim. Cosmochim. Acta 73, 923–934.

Delvigne, C., Cardinal, D., Hofmann, A., André, L., 2012. Stratigraphic changes of Ge/Si, REE + Y and silicon isotopes as insights into the deposition of a Mesoarchaean banded iron formation. Earth Planet. Sci. Lett. 355–356, 109–118.

Demarest, M.S., Brzezinski, M.A., Beucher, C.P., 2009. Fractionation of silicon isotopes during biogenic silica dissolution. Geochim. Cosmochim. Acta 73, 5572–5583.

DeMaster, D.J., 2014. 9.4 — The diagenesis of biogenic silica: chemical transformations occurring in the water column, seabed, and crust. In: Turekian, H.D.H.K. (Ed.), Treatise on Geochemistry, second ed. Elsevier, Oxford, pp. 103–111.

Ding, T., 2004. Chapter 25 — Analytical methods for silicon isotope determinations. Handbook of Stable Isotope Analytical Techniques, pp. 523–537.

Ding, T., Jiang, S., Wang, D., Li, Y., Li, J., Song, H., Lao, X., 1996. Silicon Isotope Geochemistry. Geological Publishing House.

Ding, T., Wan, D., Wang, C., Zhang, F., 2004. Silicon isotope compositions of dissolved silicon and suspended matter in the Yangtze River, China. Geochim. Cosmochim. Acta 68, 205–216.

Ding, T.P., Gao, J.F., Tian, S.H., Wang, H.B., Li, M., 2011. Silicon isotopic composition of dissolved silicon and suspended particulate matter in the Yellow River, China, with implications for the global silicon cycle. Geochim. Cosmochim. Acta 75, 6672–6689.

Emsbo, P., McLaughlin, P.I., Breit, G.N., Bray, E.A.d., Koenig, A.E., 2015. Rare earth elements in sedimentary phosphate deposits: solution to the global REE crisis? Gondwana Res. 27, 776–785.

Evans, M.J., Derry, L.A., 2002. Quartz control of high germanium/silicon ratios in geothermal waters. Geology 30, 1019.

Fan, H., Zhu, X., Wen, H., Yan, B., Li, J., Feng, L., 2014. Oxygenation of Ediacaran Ocean recorded by iron isotopes. Geochim. Cosmochim. Acta 140, 80–94.

Frei, R., Polat, A., 2007. Source heterogeneity for the major components of ~3.7 Ga banded iron formations (Isua Greenstone Belt, Western Greenland): tracing the nature of interacting water masses in BIF formation. Earth Planet. Sci. Lett. 253, 266–281.

Froelich, P.N., Hambrick, G.A., Andreae, M.O., Mortlock, R.A., Edmond, J.M., 1985. The geochemistry of inorganic germanium in natural waters. J. Geophys. Res. Atmos. 90, 1133–1141.

Froelich, P.N., Blanc, V., Mortlock, R.A., Chillrud, S.N., Dunstan, W., Udomkit, A., 1992. River fluxes of dissolved silica to the ocean were higher during glacials: Ge/Si in diatoms, rivers, and oceans. Paleoceanography 7, 739–767.

Geilert, S., Vroon, P.Z., Roerdink, D.L., Cappellen, P.V., Bergen, M.J.v., 2014a. Silicon isotope fractionation during abiotic silica precipitation at low temperatures: inferences from flow-through experiments. Geochim. Cosmochim. Acta 142, 95–114.

Geilert, S., Vroon, P.Z., van Bergen, M.J., 2014b. Silicon isotopes and trace elements in chert record early Archean basin evolution. Chem. Geol. 386, 133–142.

Geilert, S., Vroon, P.Z., Keller, N.S., Gudbrandsson, S., Stefansson, A., van Bergen, M.J., 2015. Silicon isotope fractionation during silica precipitation from hot-spring waters: evidence from the Geysir geothermal field, Iceland. Geochim. Cosmochim. Acta 164, 403–427.

German, C.R., Holliday, B.P., Elderfield, H., 1991. Redox cycling of rare earth elements in the suboxic zone of the Black Sea. Geochim. Cosmochim. Acta 55, 3553–3558.

Hamade, T., Konhauser, K.O., Raiswell, R., Goldsmith, S., Morris, R.C., 2003. Using Ge/Si ratios to decouple iron and silica fluxes in Precambrian banded iron formations. Geology 31, 35–38.

Hammond, D.E., McManus, J., Berelson, W.M., Meredith, C., Klinkhammer, G.P., Coale, K.H., 2000. Diagenetic fractionation of Ge and Si in reducing sediments: the missing Ge sink and a possible mechanism to cause glacial/interglacial variations in oceanic Ge/Si. Geochim. Cosmochim. Acta 64, 2453–2465.

Heck, P.R., Huberty, J.M., Kita, N.T., Ushikubo, T., Kozdon, R., Valley, J.W., 2011. SIMS analyses of silicon and oxygen isotope ratios for quartz from Archean and Paleoproterozoic banded iron formations. Geochim. Cosmochim. Acta 75, 5879–5891.

Hu, G.Y., Fan, F.C., Wan, D.F., Li, Y.H., Chen, S.M., 2013. Geochemistry of bedded cherts in the cap carbonates in Three Gorges Region, Hubei Province, and its paleoenvironmental implication. Acta Geol. Sin. 87, 1469–1476.

Jiang, G., Kaufman, A.J., Christie-Blick, N., Zhang, S., Wu, H., 2007. Carbon isotope variability across the Ediacaran Yangtze platform in South China: implications for a large surface-to-deep ocean $\delta^{13}C$ gradient. Earth Planet. Sci. Lett. 261, 303–320.

King, S.L., Froelich, P.N., Jahnke, R.A., 2000. Early diagenesis of germanium in sediments of the Antarctic South Atlantic: in search of the missing Ge sink. Geochim. Cosmochim. Acta 64, 1375–1390.

Knauth, L., 1994. Petrogenesis of chert. In: Heany, P.J., Prewitt, C.T., Gibbs, G.V. (Eds.), Silica: Physical Behavior, Geochemistry and Materials ApplicationsReviews in Mineralogy & Geochemistry Vol. 29. Mineralogical Society of America, Washington, DC, pp. 233–256.

Li, Y.H., Ding, T.P., Wan, D.F., 1995. Experimental study of silicon isotope dynamic fractionation and its application in geology. Chin. J. Geochem. 14, 212–219.

Li, R., Chen, J., Zhang, S., Lei, J., Shen, Y., Chen, X., 1999. Spatial and temporal variations in carbon and sulfur isotopic compositions of Sinian sedimentary rocks in the Yangtze platform, South China. Precambrian Res. 97, 59–75.

Li, C., Love, G.D., Lyons, T.W., Fike, D.A., Sessions, A.L., Chu, X., 2010. A stratified redox model for the Ediacaran ocean. Science 328, 80–83.

Li, Y.H., Hou, K.J., Wan, D.F., Zhang, Z.J., Yue, G.L., 2014. Precambrian banded iron formations in the North China Craton: silicon and oxygen isotopes and genetic implications. Ore Geol. Rev. 57, 299–307.

Ling, H.F., Chen, X., Li, D., Wang, D., Shields-Zhou, G.A., Zhu, M., 2013. Cerium anomaly variations in Ediacaran-earliest Cambrian carbonates from the Yangtze Gorges area, South China: implications for oxygenation of coeval shallow seawater. Precambrian Res. 225, 110–127.

Liu, P.J., Yin, C.Y., Chen, S.M., Tang, F., Gao, L.Z., 2013. The biostratigraphic succession of acanthomorphic acritarchs of the Ediacaran Doushantuo Formation in the Yangtze Gorges area, South China and its biostratigraphic correlation with Australia. Precambrian Res. 225, 29–43.

Liu, P.J., Chen, S.M., Zhu, M.Y., Li, M., Yin, C.Y., Shang, X.D., 2014. High-resolution biostratigraphic and chemostratigraphic data from the Chenjiayuanzi section of the Doushantuo Formation in the Yangtze Gorges area, South China: implication for subdivision and global correlation of the Ediacaran system. Precambrian Res. 249, 199–214.

Maliva, R.G., Knoll, A.H., Simonson, B.M., 2005. Secular change in the Precambrian silica cycle: insights from chert petrology. Geol. Soc. Am. Bull. 117, 835.

Marin-Carbonne, J., Chaussidon, M., Francois, R., 2010. Microscale oxygen isotope variations in 1.9 Ga Gunflint cherts: assessments of diagenesis effects and implications for oceanic paleotemperature reconstructions. Geochim. Cosmochim. Acta 74, 116–130.

Marin-Carbonne, J., Chaussidon, M., Boiron, M.-C., Robert, F., 2011. A combined in situ oxygen, silicon isotopic and fluid inclusion study of a chert sample from Onverwacht Group (3.35 Ga, South Africa): new constraints on fluid circulation. Chem. Geol. 286, 59–71.

Marin-Carbonne, J., Chaussidon, M., Robert, F., 2012. Micrometer-scale chemical and isotopic criteria (O and Si) on the origin and history of Precambrian cherts: implications for paleo-temperature reconstructions. Geochim. Cosmochim. Acta 92, 129–147.

Marin-Carbonne, J., Robert, F., Chaussidon, M., 2014. The silicon and oxygen isotope compositions of Precambrian cherts: a record of oceanic paleo-temperatures? Precambrian Res. 247, 223–234.

Mayer, L.M., Schick, L.L., Hardy, K.R., Wagai, R., McCarthy, J., 2004. Organic matter in small mesopores in sediments and soils. Geochim. Cosmochim. Acta 68, 3863–3872.

McFadden, K.A., Huang, J., Chu, X., Jiang, G., Kaufman, A.J., Zhou, C., Yuan, X., Xiao, S., 2008. Pulsed oxidation and biological evolution in the Ediacaran Doushantuo Formation. Proc. Natl. Acad. Sci. U. S. A. 105, 3197–3202.

McFadden, K.A., Xiao, S., Zhou, C., Kowalewski, M., 2009. Quantitative evaluation of the biostratigraphic distribution of acanthomorphic acritarchs in the Ediacaran Doushantuo Formation in the Yangtze Gorges area, South China. Precambrian Res. 173, 170–190.

McManus, J., Hammond, D.E., Cummins, K., Klinkhammer, G.P., Berelson, W.M., 2003. Diagenetic Ge–Si fractionation in continental margin environments: further evidence for a nonopal Ge sink. Geochim. Cosmochim. Acta 67, 4545–4557.

Meng, F., Ni, P., Schiffbauer, J.D., Yuan, X., Zhou, C., Wang, Y., Xia, M., 2011. Ediacaran seawater temperature: evidence from inclusions of Sinian halite. Precambrian Res. 184, 63–69.

Mortlock, R.A., Froelich, P.N., Feely, R.A., Massoth, G.J., Butterfield, D.A., Lupton, J.E., 1993. Silica and germanium in Pacific Ocean hydrothermal vents and plumes. Earth Planet. Sci. Lett. 119, 365–378.

Nothdurft, L.D., Webb, G.E., Kamber, B.S., 2004. Rare earth element geochemistry of Late Devonian reefal carbonates, canning basin, Western Australia: confirmation of a seawater REE proxy in ancient limestones. Geochim. Cosmochim. Acta 68, 263–283.

Nozaki, Y., Zhang, J., Amakawa, H., 1997. The fractionation between Y and Ho in the marine environment. Earth Planet. Sci. Lett. 148, 329–340.

Oelze, M., von Blanckenburg, F., Hoellen, D., Dietzel, M., Bouchez, J., 2014. Si stable isotope fractionation during adsorption and the competition between kinetic and equilibrium isotope fractionation: implications for weathering systems. Chem. Geol. 380, 161–171.

Oelze, M., von Blanckenburg, F., Bouchez, J., Hoellen, D., Dietzel, M., 2015. The effect of Al on Si isotope fractionation investigated by silica precipitation experiments. Chem. Geol. 397, 94–105.

Opfergelt, S., Cardinal, D., André, L., Delvigne, C., Bremond, L., Delvaux, B., 2010. Variations of $\delta^{30}Si$ and Ge/Si with weathering and biogenic input in tropical basaltic ash soils under monoculture. Geochim. Cosmochim. Acta 74, 225–240.

Opfergelt, S., Georg, R.B., Delvaux, B., Cabidoche, Y.M., Burton, K.W., Halliday, A.N., 2012. Silicon isotopes and the tracing of desilication in volcanic soil weathering sequences, Guadeloupe. Chem. Geol. 326–327, 113–122.

Perry Jr., E.C., Lefticariu, L., 2014. 9.5 — Formation and geochemistry of Precambrian cherts. In: Turekian, H.D.H.K. (Ed.), Treatise on Geochemistry, second ed. Elsevier, Oxford, pp. 113–139.

Pogge von Strandmann, P.A.E., Opfergelt, S., Lai, Y.-J., Sigfússon, B., Gislason, S.R., Burton, K.W., 2012. Lithium, magnesium and silicon isotope behaviour accompanying weathering in a basaltic soil and pore water profile in Iceland. Earth Planet. Sci. Lett. 339–340, 11–23.

Pokrovsky, O.S., Pokrovski, G.S., Schott, J., Galy, A., 2006. Experimental study of germanium adsorption on goethite and germanium coprecipitation with iron hydroxide: X-ray absorption fine structure and macroscopic characterization. Geochim. Cosmochim. Acta 70, 3325–3341.

Qi, L., Hu, J., DC., G., 2000. Determination of trace elements in granites by inductively coupled plasma mass spectrometry. Talanta 51, 507–513.

Raczek, I., Stoll, B., Hofmann, A.W., Peter, Jochum K., 2001. High-precision trace element data for the USGS reference materials BCR-1, BCR-2, BHVO-1, BHVO-2, AGV-1, AGV-2, DTS-1, DTS-2, GSP-1 and GSP-2 by ID-TIMS and MIC-SSMS. Geostand. Newslett. 25, 77–86.

Ramseyer, K., Amthor, J.E., Matter, A., Pettke, T., Wille, M., Fallick, A.E., 2013. Primary silica precipitate at the Precambrian/Cambrian boundary in the South Oman Salt Basin, Sultanate of Oman. Mar. Pet. Geol. 39, 187–197.

Robert, F., Chaussidon, M., 2006. A palaeotemperature curve for the Precambrian oceans based on silicon isotopes in cherts. Nature 443, 969–972.

Roerdink, D.L., van den Boorn, S.H.J.M., Geilert, S., Vroon, P.Z., van Bergen, M.J., 2015. Experimental constraints on kinetic and equilibrium silicon isotope fractionation during the formation of non-biogenic chert deposits. Chem. Geol. 402, 40–51.

Savage, P.S., Georg, R.B., Williams, H.M., Burton, K.W., Halliday, A.N., 2011. Silicon isotope fractionation during magmatic differentiation. Geochim. Cosmochim. Acta 75, 6124–6139.

Savage, P.S., Georg, R.B., Williams, H.M., Halliday, A.N., 2013. The silicon isotope composition of the upper continental crust. Geochim. Cosmochim. Acta 109, 384–399.

Shen, B., Lee, C.-T.A., Xiao, S.H., 2011. Germanium/silica ratios in diagenetic chert nodules from the Ediacaran Doushantuo Formation, South China. Chem. Geol. 280, 323–335.

Shields, G., Stille, P., 2001. Diagenetic constraints on the use of cerium anomalies as palaeoseawater redox proxies: an isotopic and REE study of Cambrian phosphorites. Chem. Geol. 175, 29–48.

Sholkovitz, E.R., Shaw, T.J., Schneider, D.L., 1992. The geochemistry of rare earth elements in the seasonally anoxic water column and porewaters of Chesapeake Bay. Geochim. Cosmochim. Acta 56, 3389–3402.

Sholkovitz, E.R., Landing, W.M., Lewis, B.L., 1994. Ocean particle chemistry: the fractionation of rare earth elements between suspended particles and seawater. Geochim. Cosmochim. Acta 58, 1567–1579.

Siever, R., 1992. The silica cycle in the Precambrian. Geochim. Cosmochim. Acta 56, 3265–3272.

Stefurak, E.J.T., Fischer, W.W., Lowe, D.R., 2015. Texture-specific Si isotope variations in Barberton Greenstone Belt cherts record low temperature fractionations in early Archean seawater. Geochim. Cosmochim. Acta 150, 26–52.

Steinhoefel, G., Horn, I., von Blanckenburg, F., 2009. Microscale tracing of Fe and Si isotope signatures in banded iron formation using femtosecond laser ablation. Geochim. Cosmochim. Acta 73, 5343–5360.

Steinhoefel, G., von Blanckenburg, F., Horn, I., Konhauser, K.O., Beukes, N.J., Gutzmer, J., 2010. Deciphering formation processes of banded iron formations from the Transvaal and the Hamersley successions by combined Si and Fe isotope analysis using UV femtosecond laser ablation. Geochim. Cosmochim. Acta 74, 2677–2696.

van den Boorn, S.H.J.M., van Bergen, M.J., Nijman, W., Vroon, P.Z., 2007. Dual role of seawater and hydrothermal fluids in Early Archean chert formation: evidence from silicon isotopes. Geology 10, 939–942.

Van den Boorn, S.H.J.M., van Bergen, M.J., Vroon, P.Z., de Vries, S.T., Nijman, W., 2010. Silicon isotope and trace element constraints on the origin of similar to 3.5 Ga cherts: implications for Early Archaean marine environments. Geochim. Cosmochim. Acta 74, 1077–1103.

Webb, G.E., Nothdurft, L.D., Kamber, B.S., Kloprogge, J.T., Zhao, J., 2009. Rare earth element geochemistry of scleractinian coral skeleton during meteoric diagenesis: a sequence through neomorphism of aragonite to calcite. Sedimentology 56, 1433–1463.

Wetzel, F., de Souza, G.F., Reynolds, B.C., 2014. What controls silicon isotope fractionation during dissolution of diatom opal? Geochim. Cosmochim. Acta 131, 128–137.

Wheat, C.G., McManus, J., 2008. Germanium in mid-ocean ridge flank hydrothermal fluids. Geochem. Geophys. Geosyst. 9, Q03025. http://dx.doi.org/10.1029/2007GC001892.

Xiao, S.H., Schiffbauer, J.D., McFadden, K.A., Hunter, J., 2010. Petrographic and SIMS pyrite sulfur isotope analyses of Ediacaran chert nodules: implications for microbial processes in pyrite rim formation, silicification, and exceptional fossil preservation. Earth Planet. Sci. Lett. 297, 481–495.

Yin, L., Zhu, M., Knoll, A., Yuan, X., Zhang, J., Hu, J., 2007. Doushantuo embryos preserved inside diapause egg cysts. Nature 446, 661–663.

Zambardi, T., Poitrasson, F., 2010. Precise determination of silicon isotopes in silicate rock reference materials by MC–ICP-MS. Geostand. Geoanal. Res. 35, 89–99.

Zhang, Y., Knoll, A.H., 1998. Permineralized fossils from the Terminal Proterozoic Doushantuo Formation, South China. J. Paleontol. (Supplement 72), 1–52.

Zhong, S., Mucci, A., 1995. Partitioning of rare earth elements (REEs) between calcite and seawater solutions at 25 °C and 1 atm, and high dissolved REE concentrations. Geochim. Cosmochim. Acta 59, 443–453.

Zhou, C., Xiao, S., 2007. Ediacaran $\delta^{13}C$ chemostratigraphy of South China. Chem. Geol. 237, 89–108.

Zhu, M., Lu, M., Zhang, J., Zhao, F., Li, G., Aihua, Y., Zhao, X., Zhao, M., 2013. Carbon isotope chemostratigraphy and sedimentary facies evolution of the Ediacaran Doushantuo Formation in Western Hubei, South China. Precambrian Res. 225, 7–28.

Ziegler, K., Chadwick, O.A., Brzezinski, M.A., Kelly, E.F., 2005. Natural variations of δ30Si ratios during progressive basalt weathering, Hawaiian Islands. Geochim. Cosmochim. Acta 69, 4597–4610.